

REPORT DOCUMENTATION PAGE			Form Approved OMB NO. 0704-0188		
<p>The public reporting burden for this collection of information is estimated to average 1 hour per response, including the time for reviewing instructions, searching existing data sources, gathering and maintaining the data needed, and completing and reviewing the collection of information. Send comments regarding this burden estimate or any other aspect of this collection of information, including suggestions for reducing this burden, to Washington Headquarters Services, Directorate for Information Operations and Reports, 1215 Jefferson Davis Highway, Suite 1204, Arlington VA, 22202-4302. Respondents should be aware that notwithstanding any other provision of law, no person shall be subject to any penalty for failing to comply with a collection of information if it does not display a currently valid OMB control number.</p> <p>PLEASE DO NOT RETURN YOUR FORM TO THE ABOVE ADDRESS.</p>					
1. REPORT DATE (DD-MM-YYYY) 13-10-2014		2. REPORT TYPE Final Report		3. DATES COVERED (From - To) 1-Jun-2010 - 31-May-2014	
4. TITLE AND SUBTITLE Final Report: Fundamental Investigation of the Microstructural Parameters to Improve Dynamic Response in Al-Cu Model System			5a. CONTRACT NUMBER W911NF-10-1-0152		
			5b. GRANT NUMBER		
			5c. PROGRAM ELEMENT NUMBER 611102		
6. AUTHORS Murat Vural, Sammy Tin			5d. PROJECT NUMBER		
			5e. TASK NUMBER		
			5f. WORK UNIT NUMBER		
7. PERFORMING ORGANIZATION NAMES AND ADDRESSES Illinois Institute of Technology 3300 South Federal Street Room 301 Main Bldg Chicago, IL 60616 -3793			8. PERFORMING ORGANIZATION REPORT NUMBER		
9. SPONSORING/MONITORING AGENCY NAME(S) AND ADDRESS (ES) U.S. Army Research Office P.O. Box 12211 Research Triangle Park, NC 27709-2211			10. SPONSOR/MONITOR'S ACRONYM(S) ARO		
			11. SPONSOR/MONITOR'S REPORT NUMBER(S) 57429-EG.4		
12. DISTRIBUTION AVAILABILITY STATEMENT Approved for Public Release; Distribution Unlimited					
13. SUPPLEMENTARY NOTES The views, opinions and/or findings contained in this report are those of the author(s) and should not be construed as an official Department of the Army position, policy or decision, unless so designated by other documentation.					
14. ABSTRACT The objective of this project is to develop an in-depth understanding of the influence of extrinsic and intrinsic microstructural parameters on dynamic response and failure behavior of Al-Cu alloys through carefully planned and fully instrumented parametric experiments and detailed microstructural characterization at various length scales. Our ultimate goal is to understand microstructural configurations that suppress the tendency of material to shear localization in the form of adiabatic shear banding (ASB). Recognizing the fact that ballistic performance is significantly improved by delaying the onset of ASD in dynamically deforming Al alloys, our approach has the					
15. SUBJECT TERMS Al-Cu alloys, Constitutive modeling, High strain rate, Adiabatic shear banding,					
16. SECURITY CLASSIFICATION OF:			17. LIMITATION OF ABSTRACT UU	15. NUMBER OF PAGES	19a. NAME OF RESPONSIBLE PERSON Murat Vural
a. REPORT UU	b. ABSTRACT UU	c. THIS PAGE UU			19b. TELEPHONE NUMBER 312-567-3181

Report Title

Final Report: Fundamental Investigation of the Microstructural Parameters to Improve Dynamic Response in Al-Cu Model System

ABSTRACT

The objective of this project is to develop an in-depth understanding of the influence of extrinsic and intrinsic microstructural parameters on dynamic response and failure behavior of Al-Cu alloys through carefully planned and fully instrumented parametric experiments and detailed microstructural characterization at various length scales. Our ultimate goal is to understand microstructural configurations that suppress the tendency of material to shear localization in the form of adiabatic shear banding (ASB). Recognizing the fact that ballistic performance is significantly improved by delaying the onset of ASB in dynamically deforming Al alloys, our approach has the potential of providing unique guidelines for developing thermal-mechanical processing techniques to obtain high performance Al alloys applicable to army mission. Improving the fundamental understanding of how intrinsic and extrinsic parameters influence the deformation substructure and overall dynamic mechanical behavior will aid in: (i) the development of new routes to tailor microstructures that promote homogeneous strain fields and demotes premature shear localization, (ii) the development of predictive constitutive models capable of accurately simulating the high strain rate deformation behavior of these materials in armor-based applications, and (iii) better understanding as well as manipulation of thermoplastic heating during severe dynamic deformation processes.

Enter List of papers submitted or published that acknowledge ARO support from the start of the project to the date of this printing. List the papers, including journal references, in the following categories:

(a) Papers published in peer-reviewed journals (N/A for none)

Received

Paper

TOTAL:

Number of Papers published in peer-reviewed journals:

(b) Papers published in non-peer-reviewed journals (N/A for none)

Received

Paper

TOTAL:

Number of Papers published in non peer-reviewed journals:

(c) Presentations

Kozmel, T., Vural, M., & Tin, S. (2014). EBSD characterization of deformation in high strain rate application aluminum alloys. In A. Bajaj, P. Zavattieri, M. Koslowski, & T. Siegmund (Eds.). Proceedings of the Society of Engineering Science 51st Annual Technical Meeting, October 1-3, 2014, West Lafayette: Purdue University Libraries Scholarly Publishing Services, 2014. <http://docs.lib.purdue.edu/ses2014/mss/mmemb/34>

Number of Presentations: 1.00

Non Peer-Reviewed Conference Proceeding publications (other than abstracts):

Received Paper

TOTAL:

Number of Non Peer-Reviewed Conference Proceeding publications (other than abstracts):

Peer-Reviewed Conference Proceeding publications (other than abstracts):

Received Paper

TOTAL:

Number of Peer-Reviewed Conference Proceeding publications (other than abstracts):

(d) Manuscripts

Received Paper

TOTAL:

Number of Manuscripts:

Books

Received Book

TOTAL:

TOTAL:

Patents Submitted

Patents Awarded

Awards

Graduate Students

NAME	PERCENT SUPPORTED	Discipline
Tom Kozmel	1.00	
FTE Equivalent:	1.00	
Total Number:	1	

Names of Post Doctorates

NAME	PERCENT SUPPORTED
FTE Equivalent:	
Total Number:	

Names of Faculty Supported

NAME	PERCENT SUPPORTED	National Academy Member
Murat Vural	0.00	
Sammy Tin	0.00	
FTE Equivalent:	0.00	
Total Number:	2	

Names of Under Graduate students supported

NAME	PERCENT SUPPORTED
FTE Equivalent:	
Total Number:	

Student Metrics

This section only applies to graduating undergraduates supported by this agreement in this reporting period

The number of undergraduates funded by this agreement who graduated during this period: 0.00

The number of undergraduates funded by this agreement who graduated during this period with a degree in science, mathematics, engineering, or technology fields:..... 0.00

The number of undergraduates funded by your agreement who graduated during this period and will continue to pursue a graduate or Ph.D. degree in science, mathematics, engineering, or technology fields:..... 0.00

Number of graduating undergraduates who achieved a 3.5 GPA to 4.0 (4.0 max scale):..... 0.00

Number of graduating undergraduates funded by a DoD funded Center of Excellence grant for Education, Research and Engineering:..... 0.00

The number of undergraduates funded by your agreement who graduated during this period and intend to work for the Department of Defense 0.00

The number of undergraduates funded by your agreement who graduated during this period and will receive scholarships or fellowships for further studies in science, mathematics, engineering or technology fields: 0.00

Names of Personnel receiving masters degrees

NAME

Total Number:

Names of personnel receiving PHDs

NAME

Total Number:

Names of other research staff

NAME

PERCENT SUPPORTED

FTE Equivalent:

Total Number:

Sub Contractors (DD882)

Inventions (DD882)

Scientific Progress

See Attachment

Technology Transfer

Final Report for Award W911NF-10-1-0152 (Proposal # 57429EG)

Report Period – Start Date: 06-01-2010 | End Date: 05-31-2014

Project Title – Fundamental Investigation of the Microstructural Parameters to Improve
Dynamic Response in Al-Cu Model System

by

Murat Vural and Sammy Tin

Illinois Institute of Technology, Chicago, IL 60616

Overview

The objective of this project is to develop an in-depth understanding of the influence of extrinsic and intrinsic microstructural parameters on dynamic response and failure behavior of Al-Cu alloys through carefully planned and fully instrumented parametric experiments and detailed microstructural characterization at various length scales. Our ultimate goal is to understand microstructural configurations that suppress the tendency of material to shear localization in the form of adiabatic shear banding (ASB). Recognizing the fact that ballistic performance is significantly improved by delaying the onset of ASB in dynamically deforming Al alloys, our approach has the potential of providing unique guidelines for developing thermal-mechanical processing techniques to obtain high performance Al alloys applicable to army mission. Improving the fundamental understanding of how intrinsic and extrinsic parameters influence the deformation substructure and overall dynamic mechanical behavior will aid in: (i) the development of new routes to tailor microstructures that promote homogeneous strain fields and demotes premature shear localization, (ii) the development of predictive constitutive models capable of accurately simulating the high strain rate deformation behavior of these materials in armor-based applications, and (iii) better understanding as well as manipulation of thermoplastic heating during severe dynamic deformation processes.

Approach

The research involves performing controlled quasi-static as well as dynamic experiments in a systematic manner over a wide range of plastic strains and high strain rates on specimens made of single crystal Al ([001] and [111] orientations), polycrystalline Al, and Al-Cu solid solution strengthened alloys (with varying Cu, Mg, Mn and Ag content). The effect of microstructural texture on dynamic deformation and failure mechanisms will be explored by testing classical as well as shear-compression specimens subjected to various thermal-mechanical processing routes. Furthermore, the dynamic thermo-mechanical response will be simultaneously measured by using state-of-the-art high-strain-rate testing techniques such as Kolsky (split Hopkinson) pressure bar in combination with well calibrated, high-speed, high-responsivity infrared (IR) detectors and fully characterized IR optics system that reliably measures the thermoplastic heat generation. The experimental data will be used to capture the evolution of thermo-mechanical coupling strength (β) as functions of thermal-mechanical processing history and microstructural texture. The data from carefully designed experiments will provide,

for the first time, critical insight into the factors that delay the onset of dynamic deformation instabilities in Al-Cu alloys such as adiabatic shear banding and the relative role of thermoplastic heating in this type of catastrophic shear instabilities. The resulting understanding will also be instrumental in developing new design guidelines for next generation Al-Cu alloys with engineered microstructures that maximize the ballistic performance.

Research Activities & Accomplishments

Research activities and accomplishments over the 4-year time span (including 1 year no-cost extension) are discussed below under the following sections: (i) material processing, (ii) rate dependent mechanical response, (iii) physics based constitutive modeling, (iv) constitutive modeling with new TVZA model, (v) adiabatic shear banding, and (vi) microstructural analysis of dynamic deformation.

(A) MATERIAL PROCESSING:

The effects of microstructure and chemistry on deformation in a series of model aluminum alloy systems were investigated in an attempt to understand the dominant features responsible for the formation of adiabatic shear bands during high strain rate deformation. In particular, the flow behavior and meso-scale deformation characteristics (on the scale of grains) under compressive loading were analyzed. Alloy chemistries were selected to isolate the various strengthening mechanisms, including the inherent crystallographic nature, the effect of grain boundaries, solid solution strengthening, as well as the many precipitate strengthening phases. Table 1 summarizes the various alloy chemistries employed, the strengthening mechanism isolated in that alloy, as well as the final state of processing for each.

Table 1: Alloy chemistries, major strengthening mechanism isolated in that alloy, and the final processed state of the alloy before testing.

Alloy (values in wt.%)	Strengthening Mechanisms	Processed State
[100] and [111] Single Crystals	Inherent crystallography	Bridgman method, 6N purity
Polycrystalline Al	Grain boundaries	Rolled and recrystallized plate
Al-0.1Cu	Solid solution	Rolled and recrystallized plate
Al-4.5Cu	Heterogeneous precipitation of θ'	Peak Aged at 160°C (320°F)
Al-4.5Cu-0.5Mg	More uniform, fine dispersion of θ'	Peak Aged at 160°C (320°F)
Al-4.5Cu-0.5Mg-0.3Mn	θ' , $\text{Al}_{20}\text{Cu}_2\text{Mn}_3$ dispersoids	Peak Aged at 160°C (320°F)
Al-4.5Cu-0.5Mg-0.3Mn-0.3Ag	All above, plus Ω precipitation	Peak Aged at 160°C (320°F)

Monocrystalline samples of ultra high purity aluminum were deformed under compression in the as-grown state. For polycrystalline aluminum samples, plates were extracted from a 99.999% purity ingot, cold rolled and recrystallized to refine the grain structure from 6-7cm to an average of 700 μm . Al-Cu alloys were melted by induction heating and cast into rectangular steel molds. Following homogenization, the ingots were

hot rolled and recrystallized to refine the grain structure; to 600 μm for the Al-0.1Cu alloy and 350 μm for Al-4.5Cu. The alloys containing Mg were processed similar to the Al-Cu alloys, but argon was used as a shielding gas during melting and homogenization, in order to prevent excessive oxidation and loss of Mg. All of the precipitation hardenable aluminum alloys were then solutioned and artificially aged at 160°C to peak hardness. This temperature was selected so that precipitation sequences begin with Guinier Preston Zone (GPZ) formation, an ideal condition for achieving optimum mechanical properties. The average grain sizes for these alloys, in the order listed in Table 1, are 250 μm , 115 μm and 100 μm respectively. Figure 1 summarizes the hardness versus aging time curves generated at 160°C, to determine the condition of peak hardness. The addition of Mn does not affect the precipitation hardenability, so the hardenability curve for this alloy was identical to that corresponding to Al-Cu-Mg and was excluded.

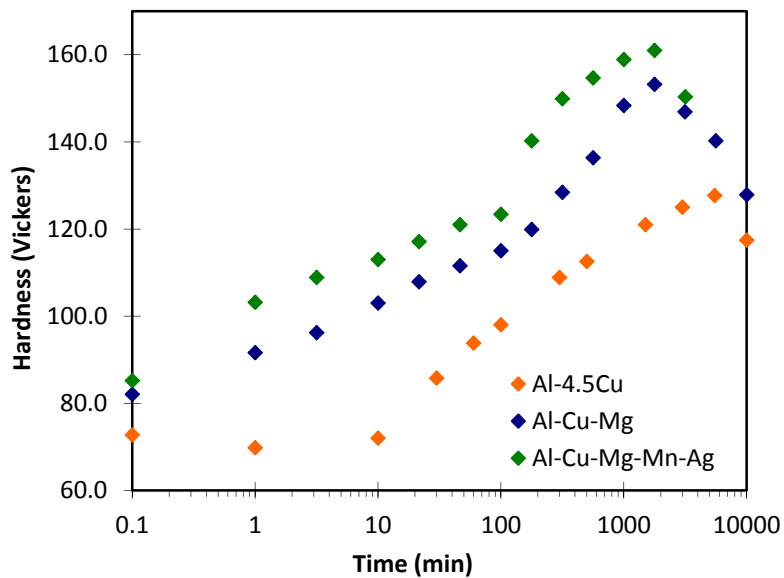


Figure 1: Artificial aging curves generated at 160°C for the various age-hardenable alloys.

Experimental Procedures: Following the processing of alloys into plate form, cylindrical compression specimens were machined parallel to the rolling direction. Sample dimensions were 7.6 mm diameter (0.3 inch) by 9.1 mm long (0.36 inch), a length-to-diameter ratio of 1.2. This study is primarily concerned with the deformation behavior as a function of strain, so all compression tests were conducted at room temperature and at a strain rate of 10^{-1} /s. Compression testing was accomplished using an Instron 1331 11,000 lb servo-hydraulic test frame. Prior to each test, a boron nitride spray lubricant was used to minimize friction between the specimen and compression anvils. Engineering flow stresses and strains were calculated directly from the load versus displacement data.

For each alloy, distinct samples were compressed to strains of 0.05, 0.1 and 0.2 for microstructural characterization. Deformed samples were sectioned parallel to the axis of deformation to reveal the center region of the compressed cylinder. Optical microscopy was used to characterize the deformed microstructures after using an orientation-sensitive anodization technique, which reveals lattice rotations and slip banding better than

conventional etching techniques. Samples were prepared by typical metallographic methods, anodized in Barker's Reagent for 2 minutes at 12 V, and imaged under polarized light at the sample center. Quantitative characterization was made possible using electron backscatter diffraction (EBSD) analysis, using a JEOL JSM-6460LV SEM outfitted with the Oxford HKL Nordlys detector and Aztec EBSD acquisition system. Analysis of the EBSD data was completed with the Oxford HKL Channel 5 software suite. EBSD was used to measure the lattice rotations and development of misorientation boundaries during deformation, to facilitate quantitative comparisons amongst the various alloys.

Results: Current results include flow stresses, optical and EBSD micrographs. Figure 2 contains the quasi-static compressive flow stress curves for all the model alloys tested at room temperature.

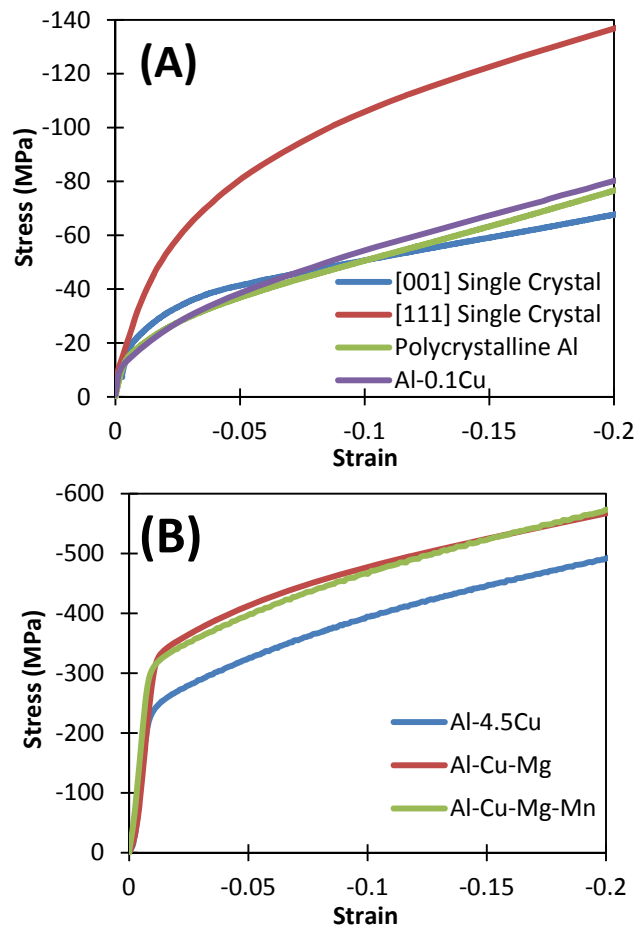


Figure 2: Flow Stress curves for the model Al alloys, a) non-age hardenable, and b) age hardenable.

Several characteristic features can be observed from these flow stress curves. First is the substantial anisotropy that exists between the single crystal Al samples loaded in the [001] and [111] crystallographic directions, with the 0.5% offset flow stress increasing from -25 MPa in the [001] loading direction to -55 MPa at [111]. The yield strengths of

the polycrystalline aluminum and Al-0.1Cu alloy are very similar to the [001] oriented single crystal, but the work hardening rates are much higher. For the single crystals, calculated strain hardening exponents are at 0.34 and 0.39 for the [001] and [111] oriented samples, whereas for the polycrystalline Al and Al-0.1Cu alloys they are much higher at 0.5. This can likely be attributed to increased dislocation interaction at grain boundaries. As expected, the age hardened alloys have substantially higher flow stresses, with a 0.5% offset yield stresses of -245 MPa, -330 MPa and -330 MPa for the Al-4.5Cu, Al-Cu-Mg and Al-Cu-Mg-Mn alloys respectively. Work hardening rates for these alloys are similar to the single crystals, with a strain hardening exponents of 0.29, 0.27 and 0.28 for Al-4.5Cu, Al-Cu-Mg and Al-Cu-Mg-Mn alloys respectively. These results indicate that the presence of precipitates lowers the work hardening rates over the higher purity polycrystalline alloys.

Optical micrographs were also taken from the center region of each sample. The imaging technique utilizes anodization and polarized light to produce an oxidation film whose thickness is sensitive to the lattice orientation. This allows the lattice rotations and slip banding within a grain to be observed as varying shades of light and dark. As an example, Figure 3 contains optical images from the center regions of deformed Al-Cu-Mg samples, along with the undeformed state.

The evolution of slip banding with strain for the Al-Cu-Mg alloy can be observed in Figure 3. At a strain of 0.05 (Figure 3b), the onset of slip banding can already be observed, emanating exclusively from triple points as noted by the arrows. At a strain of 0.1 (Figure 3c), the magnitude of slip banding becomes much more extensive, and in many grains has spread beyond triple point regions and throughout the grain. Interestingly, only a limited fraction of grains have experienced slip banding at this overall deformation strain. Since most slip bands appear to be originating from and associated with grain boundaries and triple points, regions undergoing slip banding at this low strain must be heavily influenced by interactions between the flow of neighboring grains and the geometric constraints at grain boundaries. A general alignment of slip bands in planes inclined to the deformation axis exists, indicating that the banding is a direct function of the macroscopic shear conditions. Bulk lattice rotations in several grains can also be observed at this strain, such as in the grains marked by arrows. It appears that at these low strains, bulk lattice rotations are the major meso-scale mechanism of accommodating the deformation, with slip band formation being a minor component as well.

An increase in strain to 0.2 leads to substantially heavier slip banding and more extensive lattice rotation. Most grains are fragmented by slip bands at this strain. For grains that do not yet have slip bands, deformation by grain-scale bulk rotations appears to be the predominating mechanism of accommodation. Most slip banding occurs in a random and wavy manner at this strain level, and often in intersecting directions, causing the general alignment to be much less clear than at lower strains. Slip banding is clearly the mechanism by which a majority of the cumulative strain is now accommodated. Continuity of slip across grain boundaries can be observed in some areas, as shown in Figure 4.

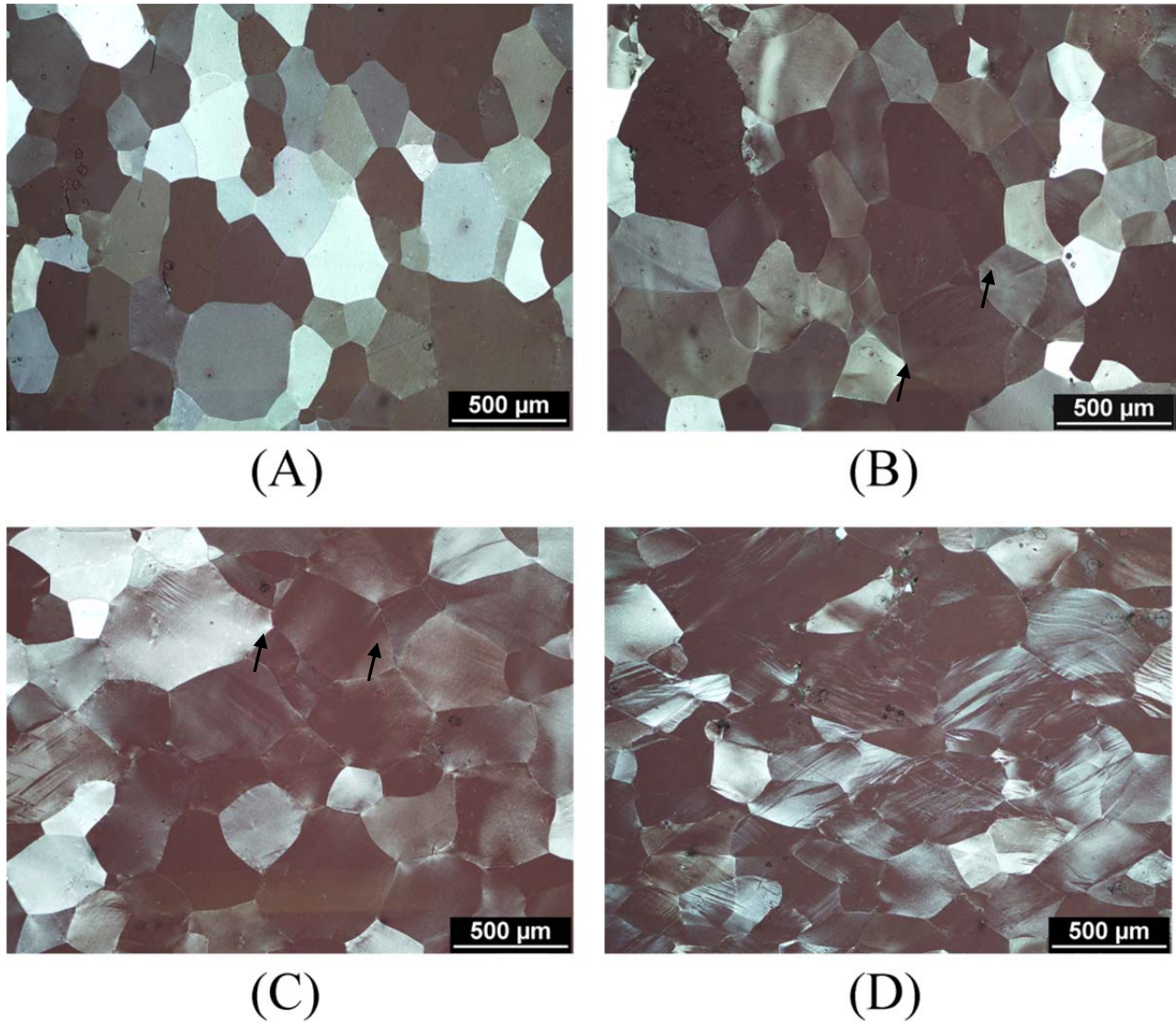


Figure 3: Optical micrographs of Al-Cu-Mg, a) annealed state, samples compressed to a strain of 0.05 (b), 0.1 (c), and 0.2 (d). Compression axis aligned vertical to the micrographs.

The complexity of slip banding at this strain may be the result of multiple levels of deformation mode within the grains. On one level is the slip banding behavior defined by the crystallographic slip within a grain, which would appear as aligned bands that spread through much of the grain. This type of slip is marked with the black arrow in Figure 4. The wavy and irregular slip bands, such as that marked by the white arrow in Figure 4, are likely the result of the geometric flow constraints necessitated by grain boundary conditions and intergranular continuity.

Since the analysis of deformed microstructures using the optical micrographs is purely qualitative, EBSD scans were extracted from the same regions of the samples for a more quantitative investigation into the deformation modes. Figure 5 contains two EBSD scans, mapped for the Al-4.5Cu alloys strained under compression to 0.05 and 0.1.

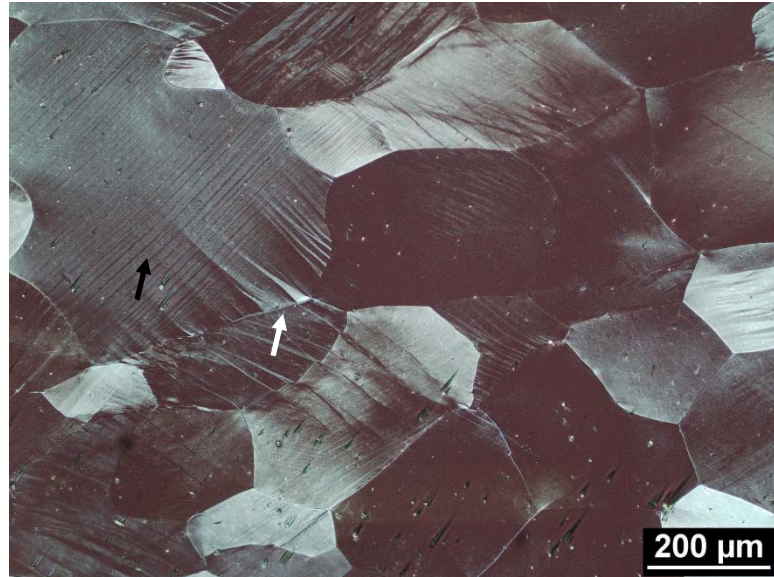


Figure 4: Magnified region of Al-Cu-Mg alloy deformed to a strain of 0.2

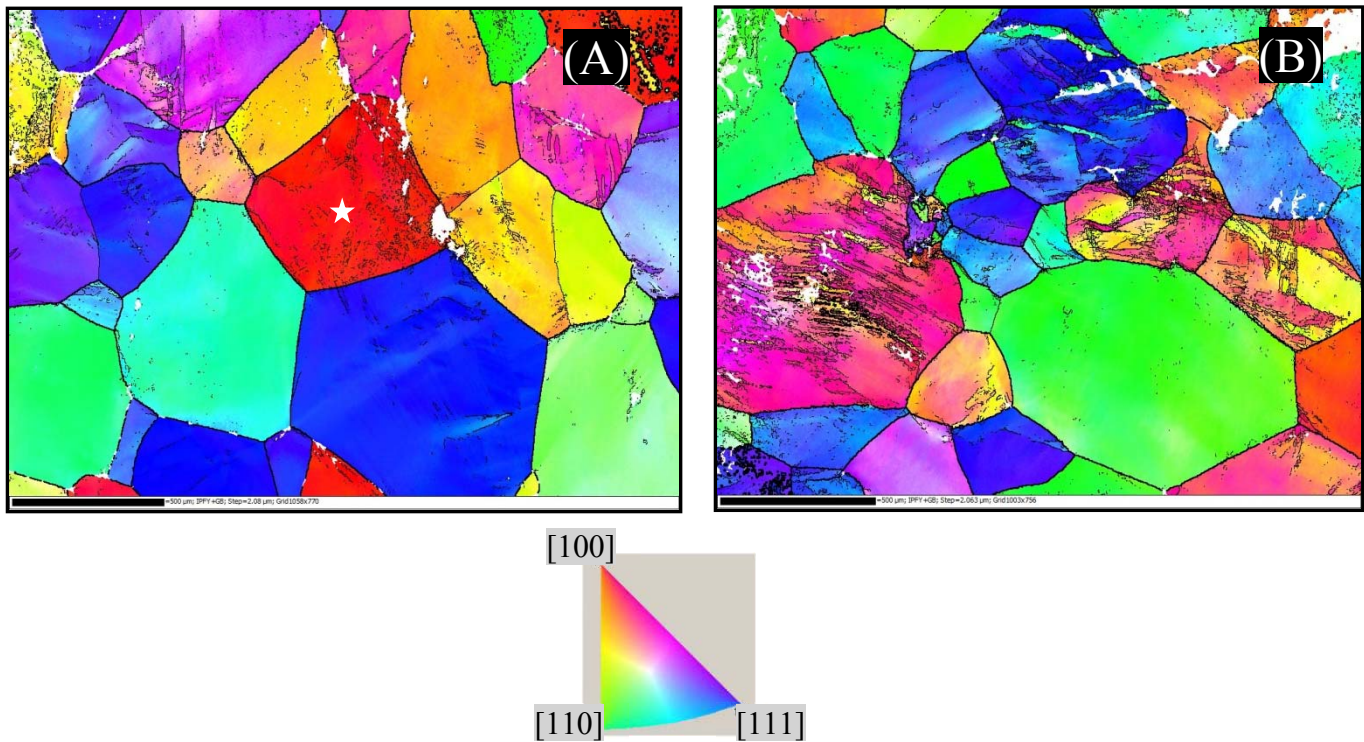


Figure 5: EBSD maps for the Al-4.5Cu alloys strained to a) 0.05, and b) 0.1. Colored based on crystallographic directions aligned with the deformation axis. Note: grain with star in Fig. 5a marked for reference in Fig. 6. Scale bars are 500μm

These EBSD maps offer detailed information into the development of lattice rotations, dislocation boundaries, and how these characteristics modes of deformation relate to the crystallography of the grains. The grain orientations that undergo higher amounts of deformation and slip banding can be identified using these maps, as well as the crystallographic rotations associated with the slip banding phenomena. The degree of intergranular lattice rotation or the level to which slip bands have developed can be quantified by the misorientation distributions measured from these maps. This allows us to quantify exactly how much a specific grain has deformed, and how developed its slip bands are at a given strain level. For example, mapping the intergranular deviations from the mean grain orientation can yield a very detailed map of the strain distribution within a grain, as shown in Figure 6 for the starred grain in Figure 5a.

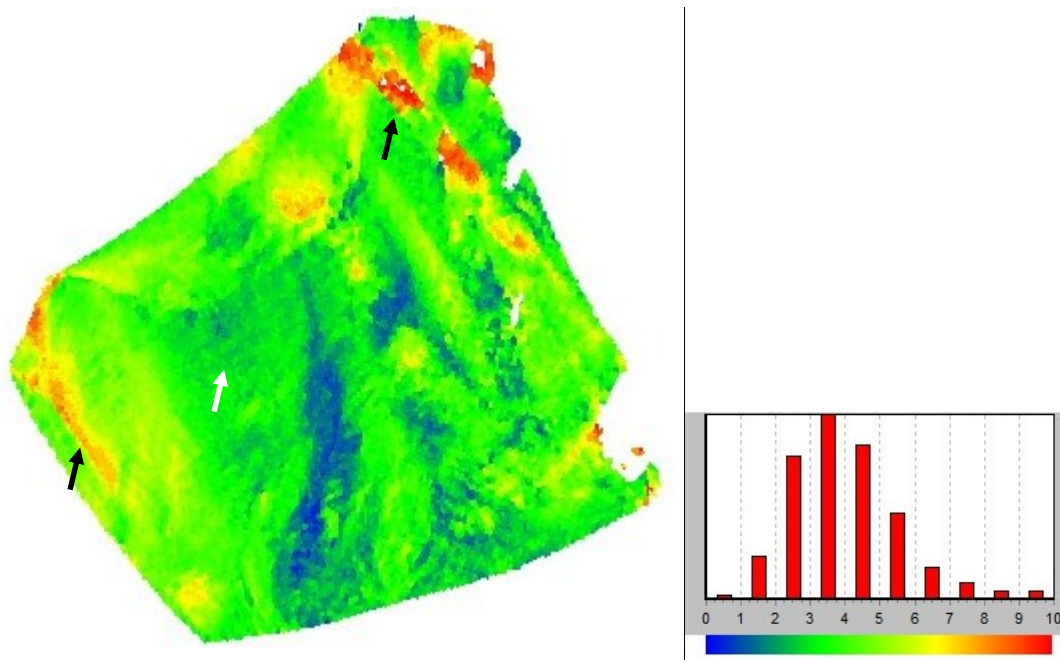


Figure 6: Map of misorientation from the average grain orientation for the grain starred in Figure 5a. Legend shows the colors corresponding to angle of misorientation from the mean grain orientation.

A map such as Figure 6 reveals the strain distribution within a singular grain. This type of map also highlights the dominant deformation behavior and heterogeneous distribution of strain accumulating within the grains. The black arrows indicate regions of heavy slip banding, with misorientations near 10° developing within the band. Such high misorientations indicate a high level of dislocation activity and strain concentration within these regions of the grain. The white arrow points to aligned slip bands that are just beginning to form at the relatively low levels of strain within the grain. These features are otherwise not visible in the optical images, since they are associated with minor dislocation activity and the early stages of band formation. The grain in Figure 6 has an average misorientation from its mean of 4° , with other grains in the same sample having values as high as 9° . This value is expected to increase with increasing levels of strain, becoming very substantial as slip banding develops more extensively at strains of

0.2. It is also expected that certain grain orientations will experience much higher levels of intergranular misorientation than others, due to the crystallographic anisotropy observed in Figure 2.

(B) RATE DEPENDENT MECHANICAL RESPONSE:

Mechanical characterization studies cover quasi-static ($10^{-4} < \dot{\epsilon} < 10^0 \text{ s}^{-1}$) as well as high-strain-rate ($10^2 < \dot{\epsilon} < 10^4 \text{ s}^{-1}$) experiments by using split Hopkinson pressure bar (SHPB) technique at room temperature and elevated temperatures. One of the objectives is to model rate and temperature dependent constitutive response of Al-Cu alloys subjected to varying thermal-mechanical processing routes while the other is to investigate the susceptibility of each alloy composition and microstructure to localized shear instabilities under dynamic loading conditions. Future phases of project also involve investigating the effect of intrinsic and extrinsic material properties on the fraction of plastic work converted into heat at high strain rates. Progress made so far in the second year of project is outlined in the following paragraphs.

To form a baseline for subsequent evaluation of constitutive response in Al-Cu alloy systems the stress-strain response of single crystal Al has been investigated over a wide range of strain rates from 10^{-3} s^{-1} to 10^3 s^{-1} . In these experiments, single crystal specimens of cylindrical shape have been subjected to uniaxial compression along [111] and [001] directions, whose results are shown in Fig. 7. Flow stress of single crystal Al in [111] direction is higher almost by a factor of 2 than that of [001] direction at corresponding strain rates. This is more than the factor of 1.5 that one would expect from the analysis of Schmid factors for potential slip systems. It is also obvious from dynamic test results that single crystals exhibit a significant strain rate hardening irrespective of the crystal orientations investigated, which results in an almost two fold increase in flow stress when the strain rate is increased from 10^{-3} s^{-1} to 10^3 s^{-1} .

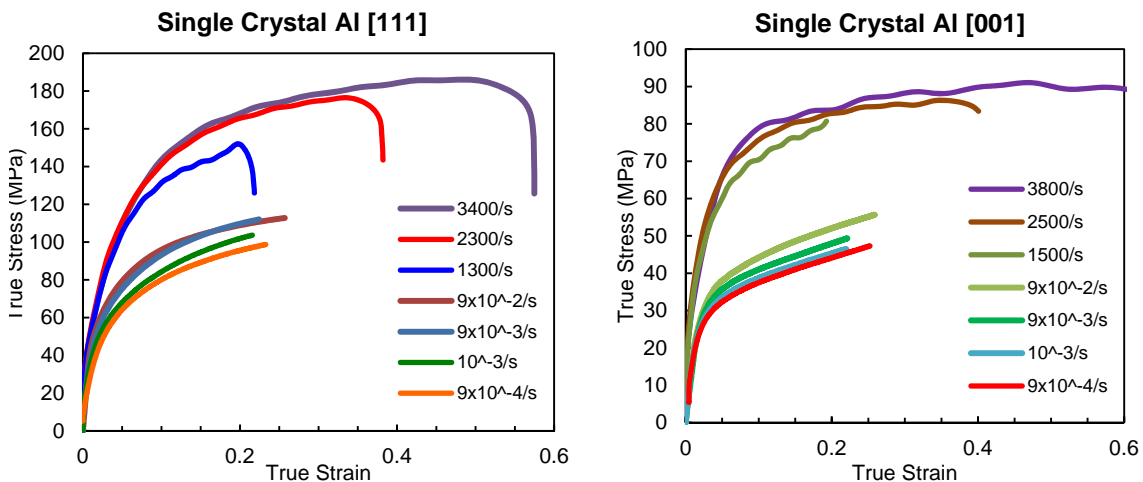


Fig. 7 Stress-strain plots of single crystal Al specimens loaded in [111] and [001] directions at varying quasi-static and dynamic strain rates.

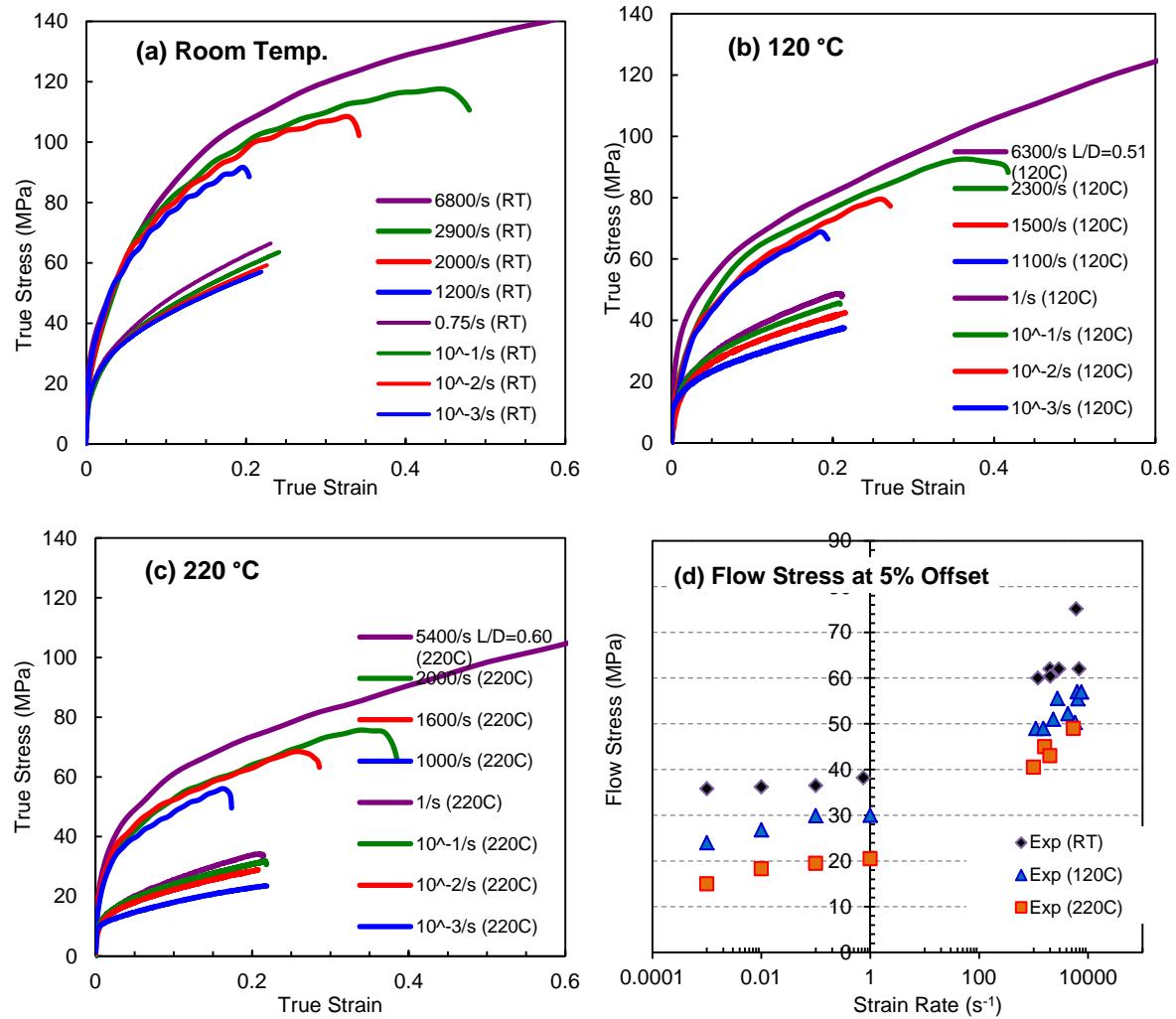


Fig. 8 Rate and temperature dependence of flow stress in pure (99.999%) polycrystalline Al.

Following the characterization of single crystal behavior, the rate and temperature dependent mechanical response of commercially pure polycrystalline Al has been completed between room temperature (RT) and 220 °C, whose results are presented in Fig. 8. Flow stress of polycrystalline Al is found to be fairly close to that of single crystal Al loaded along [001] direction at early stages of plastic deformation (up to 7% strain) while it shows a higher strain hardening at larger strains. This trend becomes more pronounced at high strain rates. At high strain rates, although single crystal Al loaded in [001] direction exhibit an almost constant flow stress beyond 10% strain, the polycrystalline material experience a significant strain hardening at similar high strain rates. This suggests that, in addition to strain hardening effect of grain boundaries, the existence of grain boundaries alters the kinetics of rate coupling possibly by preventing the saturation of dislocation density as the deformation progress.

Effect of temperature seems to be more complex than stating the obvious fact that flow stress decreases with increasing temperature. At quasi-static strain rates, temperature increase causes a monotonic decrease in strain hardening. But at high strain rates, strain

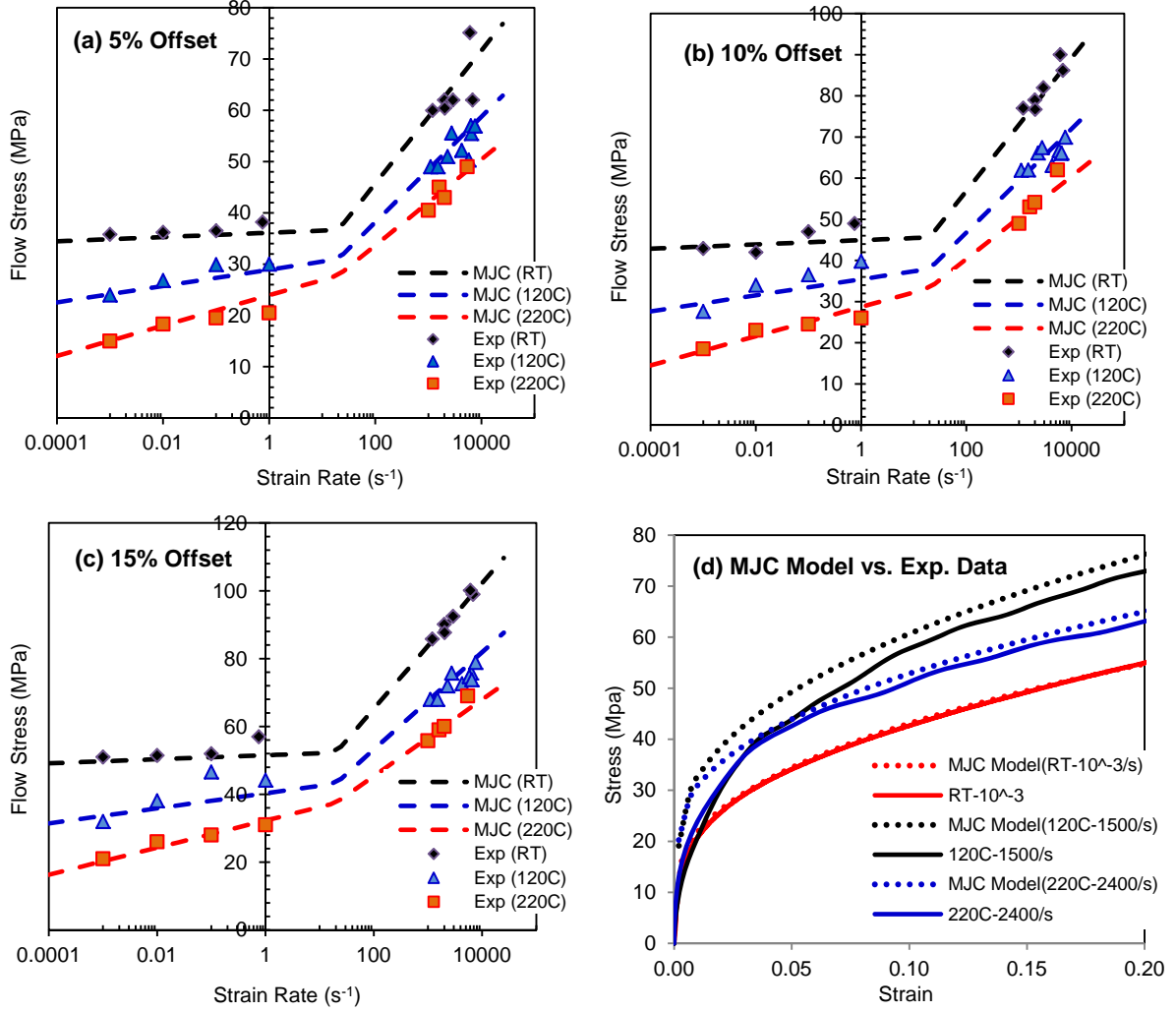


Fig. 9 Validation of the modified Johnson-Cook (MJC) model developed for the polycrystalline aluminum with experimental data. Even at 5% strain offset, the MJC model perfectly captures the material behavior. The parameters for the MJC model are given at Table 2 (see Appendix A for MJC model's details).

hardening remains almost the same until 220 °C, at which temperature only a slight decrease in strain hardening is observed. Strain rate hardening of polycrystalline structure is similar to the one observed for single crystals, i.e., an increase in flow stress by almost a factor of 2 is measured when the strain rate is increased from $10^{-3} s^{-1}$ to $10^3 s^{-1}$.

In order to account for the complex effect of temperature on strain hardening and strain rate hardening, certain modifications to commonly used Johnson-Cook model has been proposed. Essential features of this modified Johnson-Cook (MJC) model are briefly presented in Appendix A. Figure 9 shows the validation of MJC model with the experimental data for polycrystalline aluminum in a wide range of strain rates and temperatures. Corresponding MJC model parameters are presented in Table 2.

Table 2: Modified Johnson-Cook (MJC) model parameters for commercially pure aluminum.

Parameters:	q	σ_0 (Mpa)	Bo (Mpa)	To (K)	Tm (K)	p
	2.9	14.5	140	175	780	1
Parameters:	n	C1	C2	$\dot{\epsilon}_{01}$ (1/s)	$\dot{\epsilon}_t$ (1/s)	k
	0.45	0.0052	0.1565	0.001	20	400

Effect of 0.1% Cu addition to pure aluminum on flow stress is shown in Figure 10 for various temperatures. Mechanical response of Al-0.1%Cu alloy is very similar to polycrystalline aluminum, and the effect of 0.1% Cu addition is very minimal in flow stress values. Comparison of the stress-strain plots of Al-0.1%Cu with those of pure aluminum in Figure 11 reveals that 0.1% Cu addition doesn't elevate the flow stress significantly since the solid solution obtained is not age hardenable. The MJC model parameters obtained for Al-0.1% Cu alloy are presented in Table 3.

Table 3: Modified Johnson-Cook (MJC) model parameters for Al-0.1%Cu.

Parameters:	q	σ_0 (Mpa)	Bo (Mpa)	To (K)	Tm (K)	p
	3.9	5.5	112	41	670	3
Parameters:	n	C1	C2	$\dot{\epsilon}_{01}$ (1/s)	$\dot{\epsilon}_t$ (1/s)	k
	0.36	0.0068	0.2065	0.001	150	400

Figure 12 shows the MJC model fit to the experimental data for Al-0.1%Cu alloy. The MJC model is successful in capturing the material behavior and this figure also shows the similarity between polycrystalline aluminum and Al-0.1%Cu alloy in their strain rate hardening behavior at various temperatures.

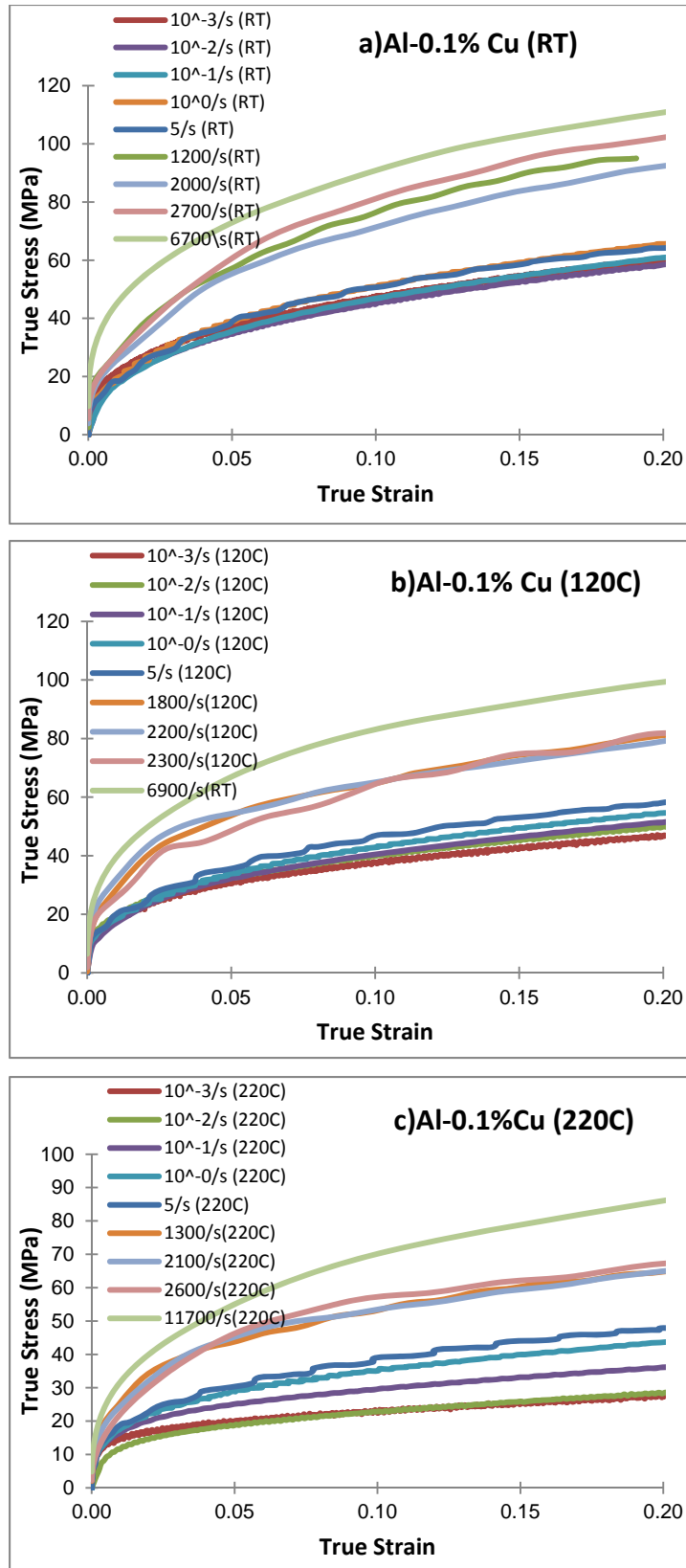


Fig. 10 Stress-strain plots of Al-0.1%Cu as a function of strain rate at (a) room temperature (RT), (b) 120 °C, and (c) 220 °C.

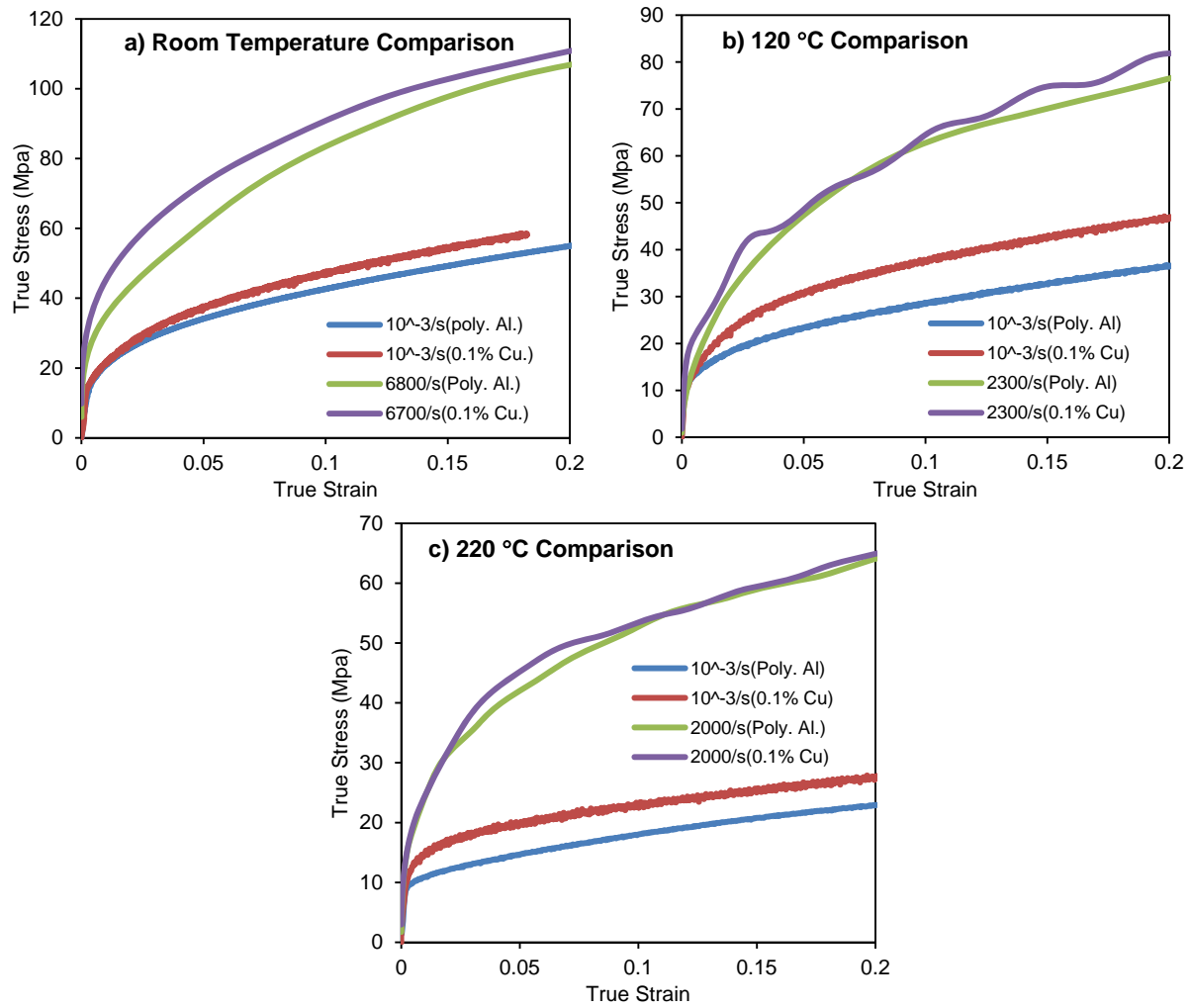


Fig. 11 Comparison of commercially pure polycrystalline aluminum (Poly. Al) with Al-0.1%Cu (0.1%Cu) at various temperatures and strain rates does not show any significant change in flow stress.

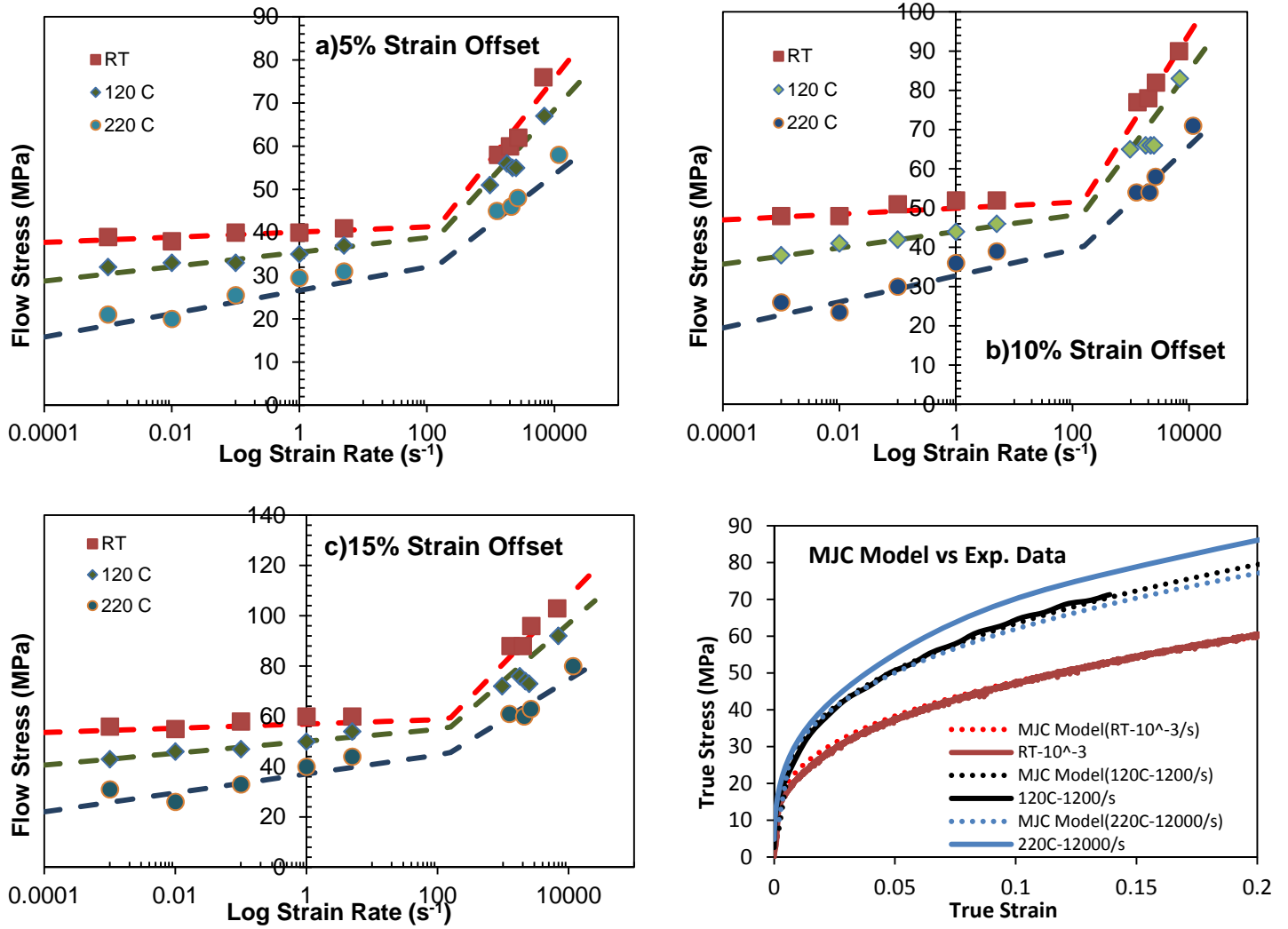


Fig. 12 Validation of the modified Johnson-Cook (MJC) model developed for Al-0.1%Cu with experimental data. The parameters for the MJC model are given at Table 3 (see Appendix A for MJC model's details).

Initial experiments that have been conducted on Al-4.5%Cu and Al-4.5%Cu-0.5%Mg-0.3%Mn alloys showed a significant amount of scatter in the experimental data. It has been concluded that this is mainly because of microstructural nonuniformity in specimens extracted from the different locations of the rolled plates. Therefore, we have altered the specimen extraction process by paying ultimate attention to potential nonuniformities in specimens their respective locations within the processed plates. Results of room temperature SHPB tests are presented in Fig. 13 for Al-4.5%Cu, which doesn't shows any significant strain rate sensitivity within the range of strain rates investigated up to 3000 s^{-1} .

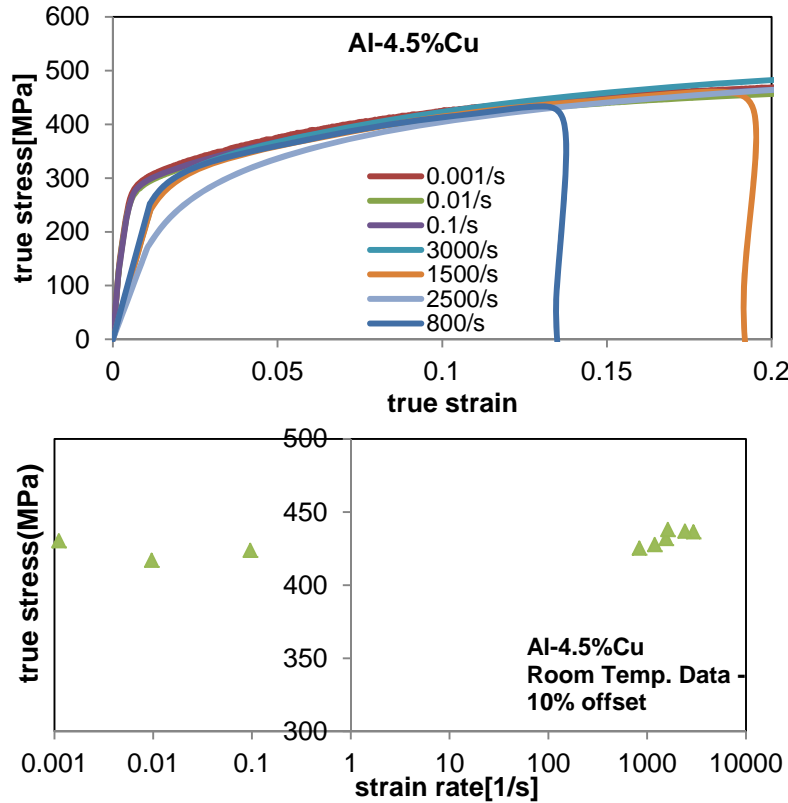


Figure 13. Room temperature experimental data for Al-4.5%Cu reveal that flow stress doesn't show any significant change up to strain rates of 3000/s..

The next alloy is obtained by adding 0.5%Mg (by weight) to the Al-4.5%Cu alloy. The θ' precipitations that were previously formed by the addition of the 4.5%Cu becomes more uniform with the addition of Mg, and the new alloy exhibits significantly higher dynamic flow stress than the Al-4.5%Cu alloy as shown in Fig. 14.

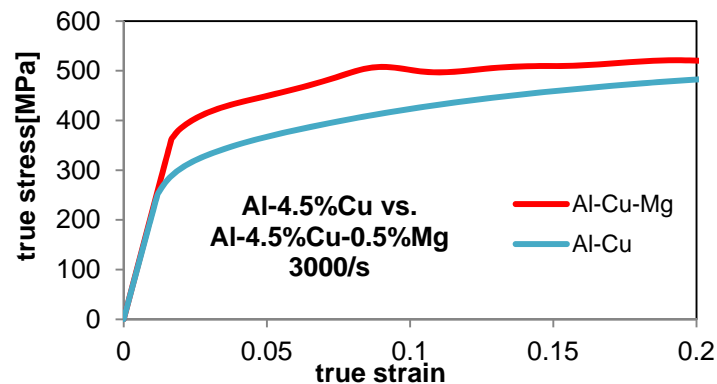


Figure 14. Comparison of Al-4.5%Cu and Al-4.5%Cu-0.5%Mg at the same high strain rate. Addition of the Mg increases dynamic flow stress.

Evolution of flow stress with strain rate and temperature is presented in Fig. 15 for Al-4.5%Cu-0.5%Mg. Although the flow stress is elevated by the addition of 0.5%Mg, it

doesn't show any significant strain rate hardening up to 3000/s, which is similar to the observations made for Al-4.5%Cu.

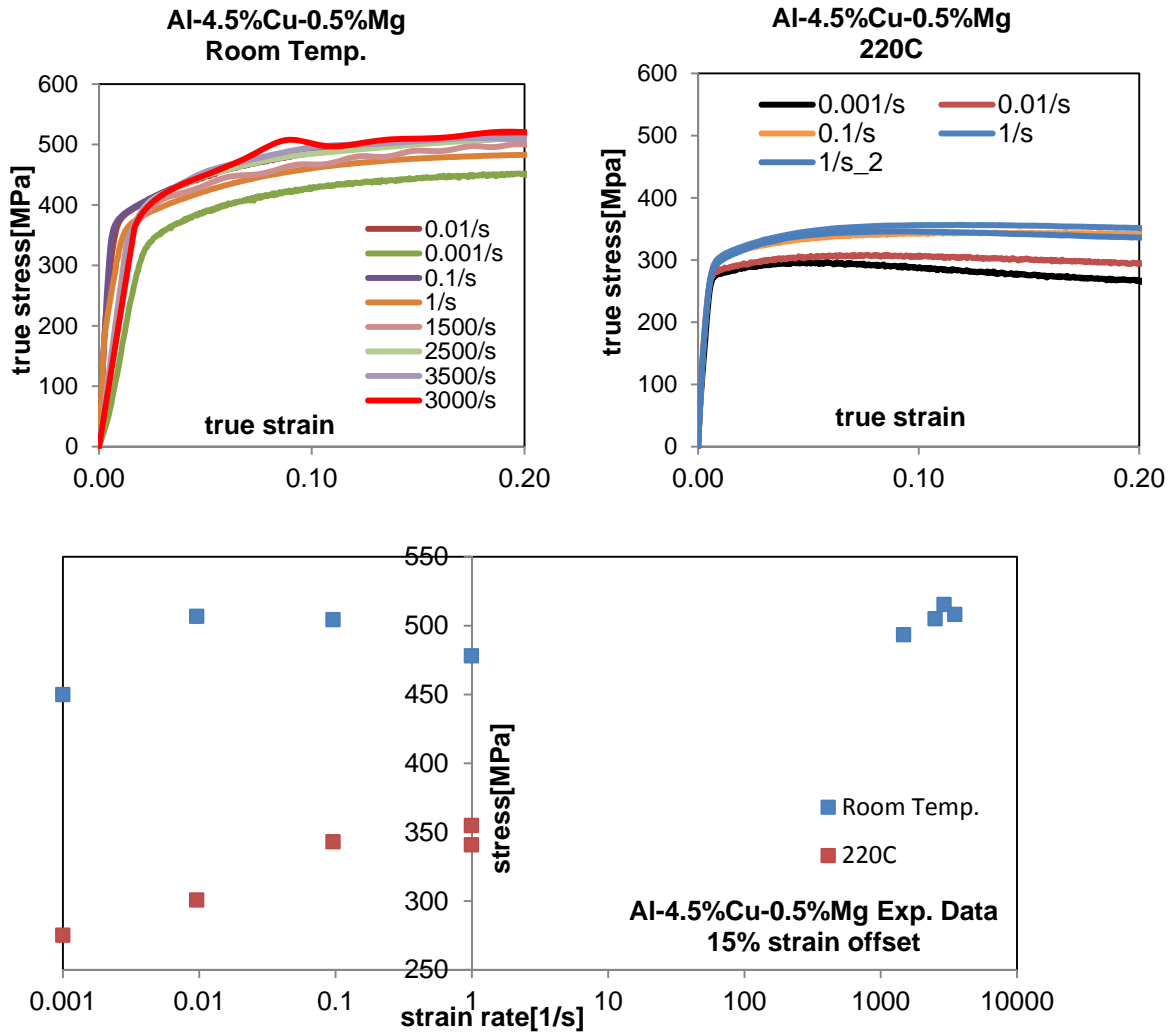


Figure 15. Current progress in Al-4.5%Cu-0.5%Mg alloy is presented. Since only strain rates up to 3000/s have been covered, flow stress values in dynamic regime are not very different from the quasi-static flow stress values. Only quasi-static data is available at 220° C.

The next step was the addition of Mn (0.3% by weight) to Al-4.5%Cu-0.5%Mg alloy, which resulted in $\text{Al}_{20}\text{Cu}_2\text{Mn}_3$ dispersoids in addition to the θ' precipitates in the microstructure. This slightly increased the average flow stress as compared to Al-4.5%Cu-0.5%Mg alloy as shown in Fig. 16 and Fig. 17.

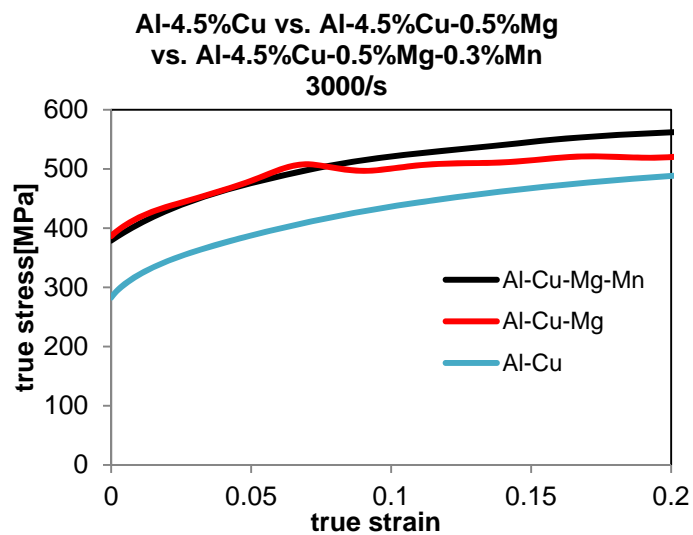


Figure 16. Comparison of the last three alloys in the dynamic regime. Al-4.5%Cu-0.5%Mg-0.3%Mn alloy has the highest flow stress values.

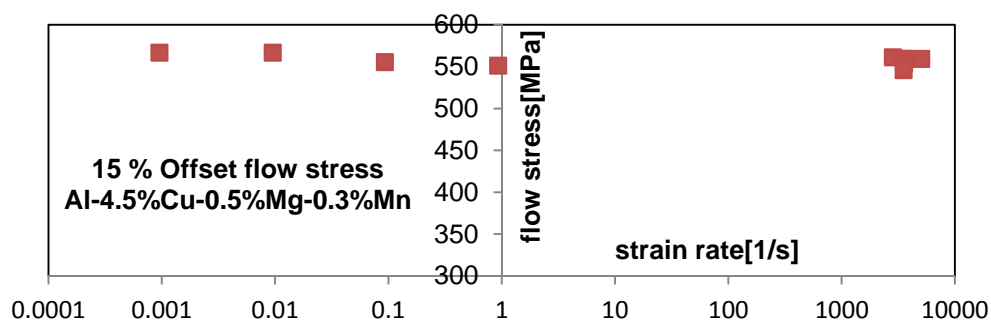
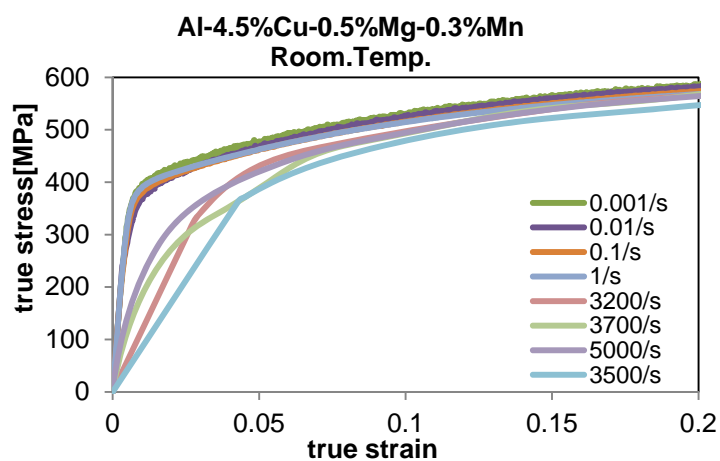


Figure 17. Room temperature data for the Al-4.5%Cu-0.5%Mg-0.3%Mn alloy.

Finally, the most complex alloy structure that mimics Al 2139 alloy composition was obtained with the addition of Ag element, which resulted new Ω precipitations in addition to $\text{Al}_{20}\text{Cu}_2\text{Mn}_3$ dispersoids and θ' precipitates that already existed in Al-4.5%Cu-0.5%Mg-0.3Mn alloy. Figure 18 shows the mechanical response of this final alloy as functions of temperature and strain rate.

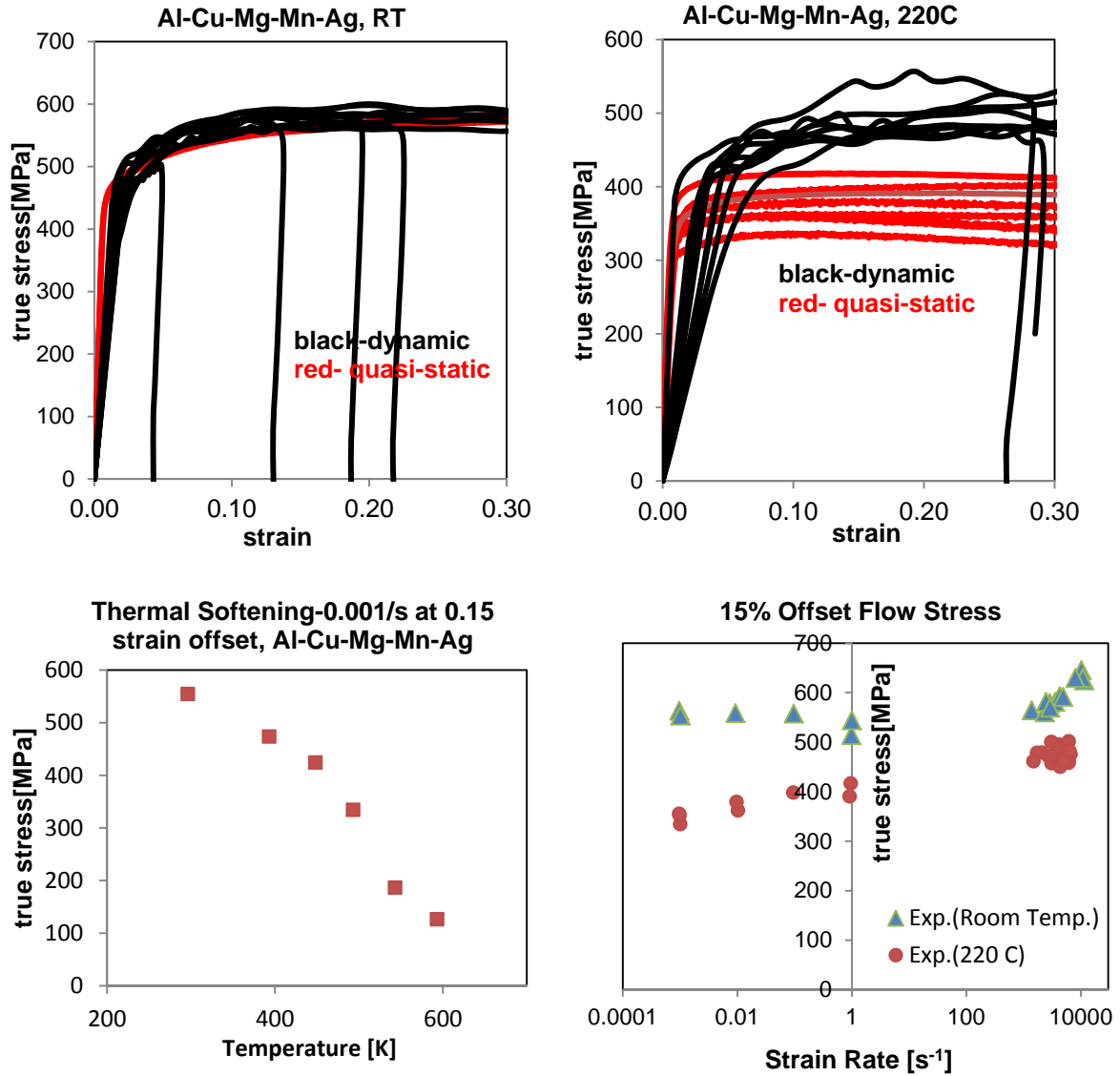


Figure 18. RT and 220°C experimental data are presented at the upper row for Al-Cu-Mg-Mn-Ag. Lower left graph shows the thermal softening behavior while the lower right graph shows the effect of strain rate and temperature on flow stress.

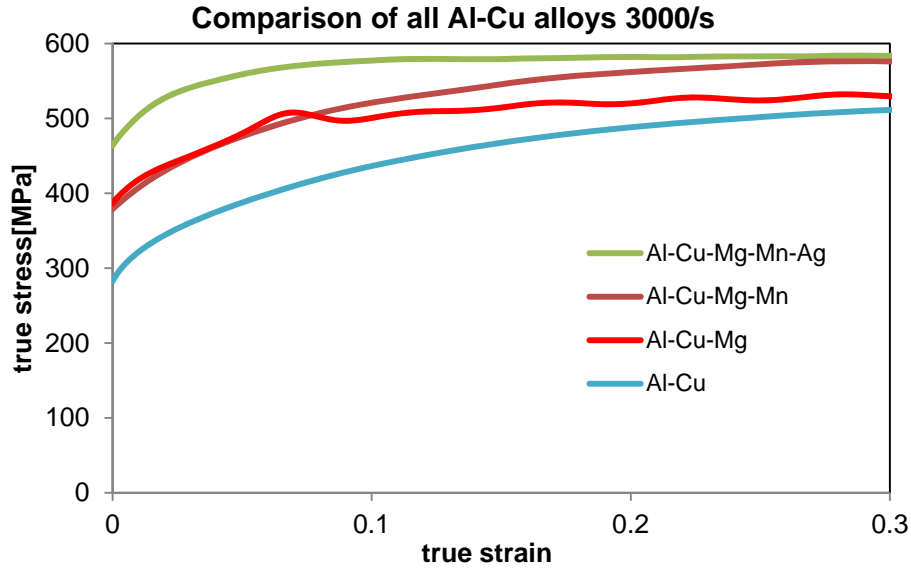


Figure 19. Al-4.5%Cu 0.5%Mg-0.3%Mn -0.3%Ag alloy has the highest flow stress values among the other Al-Cu alloys. However, beyond a strain level of about 0.3, Al-4.5%Cu-0.5%Mg-0.3%Mn reaches the same flow stress value as the Ag alloy.

Overall comparison of the flow stress of Al-Cu alloys produced in house can be seen in Fig. 19. It is obvious that the alloy Al-4.5%Cu-0.5%Mg-0.3%Mn-0.3%Ag has the highest flow stress values among the alloys that has been investigated in this study.

(C) PHYSICS BASED CONSTITUTIVE MODELING:

It has already been shown in previous section as well as in Appendix A that constitutive response of Al-Cu alloys can be satisfactorily predicted by phenomenological models such as the modified Johnson-Cook (MJC) model. It is important to note that rather simple mathematical structure of original JC model doesn't lend itself to capturing the complex dependence of strain and strain rate hardening on temperature, which is observed in all Al alloys investigated here. Therefore, modifications to original JC model have been proposed to describe their constitutive response.

In this section, we will outline our effort to develop a physics based constitutive model capable of representing the rate and temperature dependent mechanical response of complex Al-Cu alloys. Although the backbone of this effort is based on Zerilli-Armstrong (ZA) model it includes significant modifications driven by experimental data as well as further dislocation mechanics based approaches employed in other physics based models such as the MTS model.

The ZA model is based on simplified dislocation mechanics. The latest version of this model for FCC materials, which includes both Peierls stress type interactions and forest-dislocations type interactions, predicts the flow stress of material as follows:

$$\sigma = \sigma_a + B e^{-\beta T} + B_0 \varepsilon^{\frac{1}{2}} e^{-\alpha T}$$

where

$$\begin{aligned}\alpha &= \alpha_0 - \alpha_1 \ln(\dot{\varepsilon}) \\ \beta &= \beta_0 - \beta_1 \ln(\dot{\varepsilon}) \\ \sigma_a &= \frac{k}{\sqrt{l}} + \sigma_s\end{aligned}$$

Similarly, Mechanical Threshold Stress (MTS) model is a dislocation mechanics based constitutive model which incorporates mechanical threshold stress as a state variable. After recent modifications, the latest form of the MTS model is given by:

$$\sigma = \sigma_a + (S_i \sigma_i + S_e \sigma_e) \frac{\mu(p, T)}{\mu_0}$$

where scaling factors, S_i and S_e , have the Arrhenius form:

$$\begin{aligned}S_i &= \left\{ 1 - \left[\frac{kT \ln \left(\frac{\dot{\varepsilon}_{oi}}{\dot{\varepsilon}} \right)}{g_{oi} \mu b^3} \right]^{\frac{1}{q_i}} \right\}^{\frac{1}{p_i}} \\ S_e &= \left\{ 1 - \left[\frac{kT \ln \left(\frac{\dot{\varepsilon}_{oe}}{\dot{\varepsilon}} \right)}{g_{oe} \mu b^3} \right]^{\frac{1}{q_e}} \right\}^{\frac{1}{p_e}}\end{aligned}$$

And the hardening is expressed as:

$$\begin{aligned}\frac{d\sigma_e}{d\varepsilon} &= \theta_0 [1 - F(\sigma_e)] + \theta_1 F(\sigma_e) \\ \theta_0 &= a_{00} + a_{10} \ln \dot{\varepsilon} + a_{20} \sqrt{\dot{\varepsilon}} + a_{30} T \\ \theta_1 &= a_{01} + a_{11} \ln \dot{\varepsilon} + a_{21} \sqrt{\dot{\varepsilon}} + a_{31} T \\ F(\sigma_e) &= \frac{\tanh \left(\alpha \frac{\sigma_e}{\sigma_s} \right)}{\tanh(\alpha)} \\ \ln \left(\frac{\dot{\varepsilon}}{\dot{\varepsilon}_{s0}} \right) &= \frac{\mu b^3 A}{kT} \ln \left(\frac{\sigma_{es}}{\sigma_{e0s}} \right)\end{aligned}$$

Although the modified Johnson-Cook (MJC) model excels at capturing material behavior, it has no physical roots. MTS model seems as an ideal candidate for this task; however it has its shortcomings. To describe the evolution of threshold stress in the MTS model with strain rate and temperature, strain rate jump tests must be conducted. After each dynamic test with stop rings, the specimens must be re-machined as soon as possible to conduct quasi-static tests without any room temperature annealing. Therefore, it would

take considerably more time to complete the tests required for MTS model compared to the simpler tests required for other material models. Meanwhile it has more than fifteen model parameters, which makes it quite challenging to fit all parameters computationally without in advance assumption involving the magnitude of some parameters.

Even though the ZA model is considerably simpler than the MTS model, our studies show that it doesn't lend itself to model complex Al-Cu alloys mainly due to its hardening term. The ZA model has a power-law hardening term of the form $B_0 \epsilon^{\frac{1}{2}} e^{-\alpha T}$, thus flow stress is proportional to the square root of strain. However, Al-Cu alloys with complex microstructures show rather quick saturation in flow stress beyond a certain strain (see Fig. 20). Therefore, hardening parameter in the ZA model needs to be modified as will be discussed in following paragraphs.

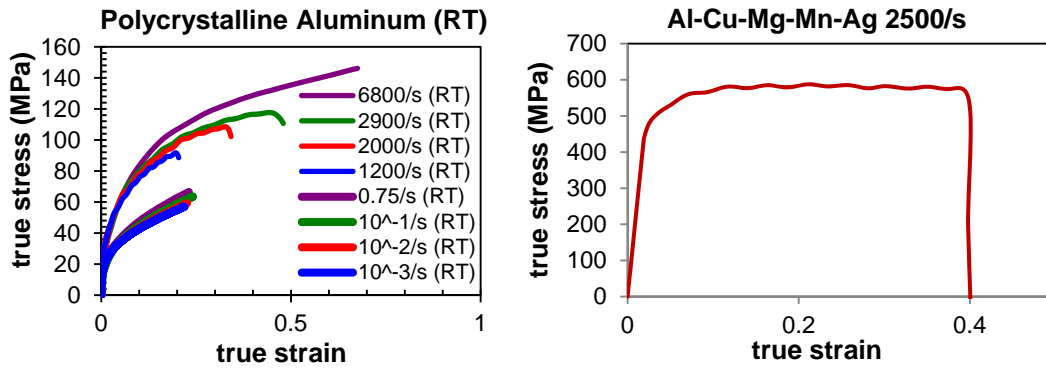


Figure 20. Polycrystalline aluminum shows hardening behavior akin to ZA model's hardening parameter, whereas more complex Al-Cu alloys show decreasing hardening rate with increasing strain rate.

Another shortcoming of the original Zerilli-Armstrong model is that it cannot capture increased rate sensitivity observed in the Al-Cu-Mg-Mn-Ag alloy beyond a strain rate of about 1000/s in the dynamic regime as shown in Fig. 21.

To overcome the difficulty of modeling materials that show hardening saturation, Zerilli and Armstrong proposed a set of modifications to the original ZA model to include dynamic recovery process. The modified ZA (MZA) model can be expressed as:

$$\sigma = \sigma_a + \sigma^*$$

$$\sigma^* = 0.5\sigma_{th} \left[1 + \left(1 + \frac{4c_0 \dot{\epsilon} T}{\sigma_{th}} \right)^{\frac{1}{2}} \right]$$

$$\sigma_{th} = B e^{-\beta T} + \left[\alpha \mu \sqrt{\frac{b}{\lambda}} \sqrt{\frac{1}{\omega} (1 - e^{-\omega \epsilon})} \right] e^{-\alpha T}$$

where

$$\alpha = \alpha_0 - \alpha_1 \ln(\dot{\epsilon})$$

$$\beta = \beta_0 - \beta_1 \ln(\dot{\epsilon})$$

With these modifications, the MZA model can finally capture the increased strain-rate sensitivity in the dynamic regime. As shown in Fig. 22, the MZA model can accurately capture the experimental data in both quasi-static and dynamic regimes at room temperature and 220° C. Although the equations seem to work pretty well for the data obtained at two distinct temperatures (RT and 220C, Fig. 22), the MZA model fails to capture the true nature of thermal softening observed in complex Al-Cu alloys. In both original ZA model and MZA model, thermal softening of flow stress is realized via exponential terms, which result in quite unrealistic softening behavior for alloys with complex microstructures (see Fig. 23). It is obvious that the exponential relation between the flow stress and the temperature must be altered to accurately capture the experimental data in a wide temperature range.

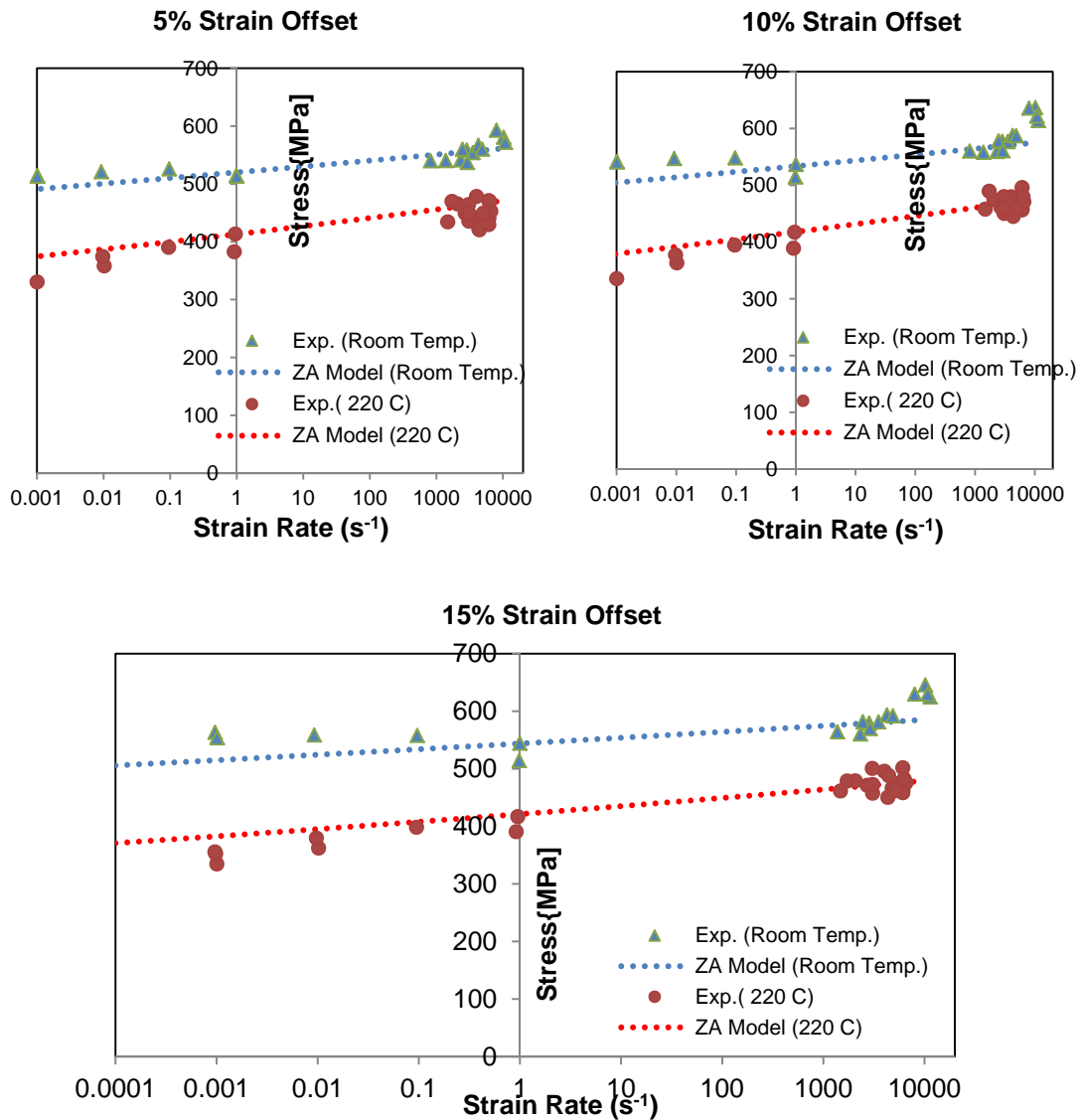


Figure 21. Original Zerilli-Armstrong Model is used to model the Al-Cu-Mg-Mn-Ag alloy. Model fails to capture the increased strain-rate sensitivity in the dynamic regime.

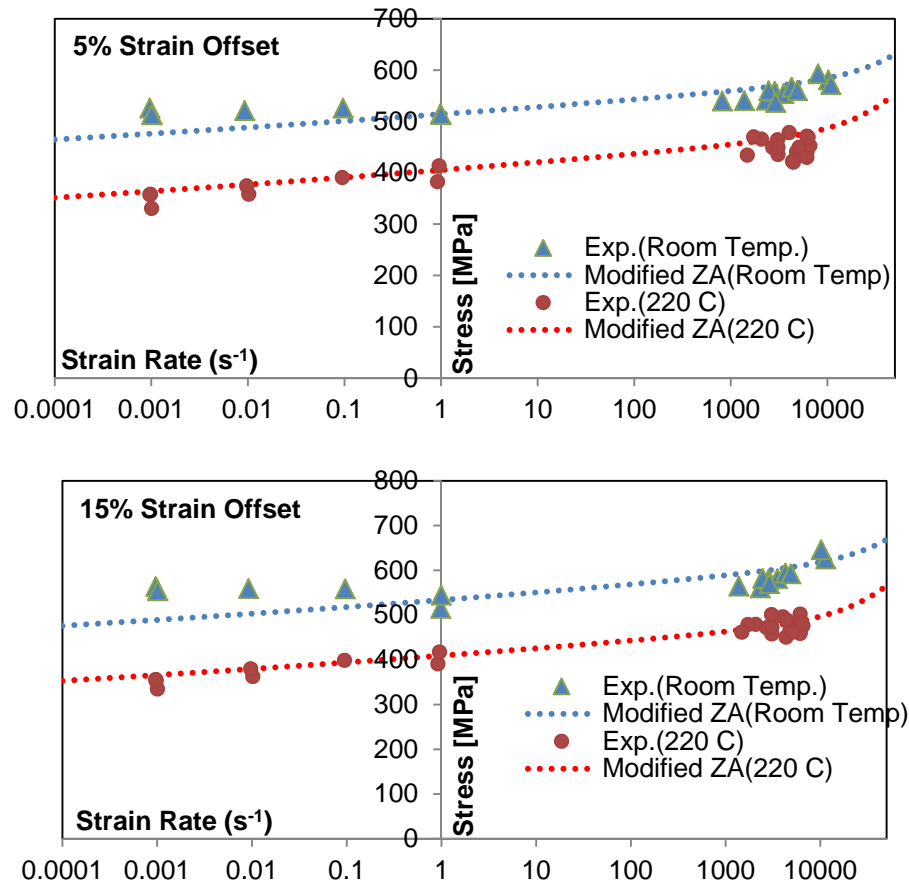


Figure 22. Al-Cu-Mg-Mn-Ag alloy modeled with Modified Zerilli-Armstrong Model which shows increased strain-rate sensitivity in the dynamic regime.

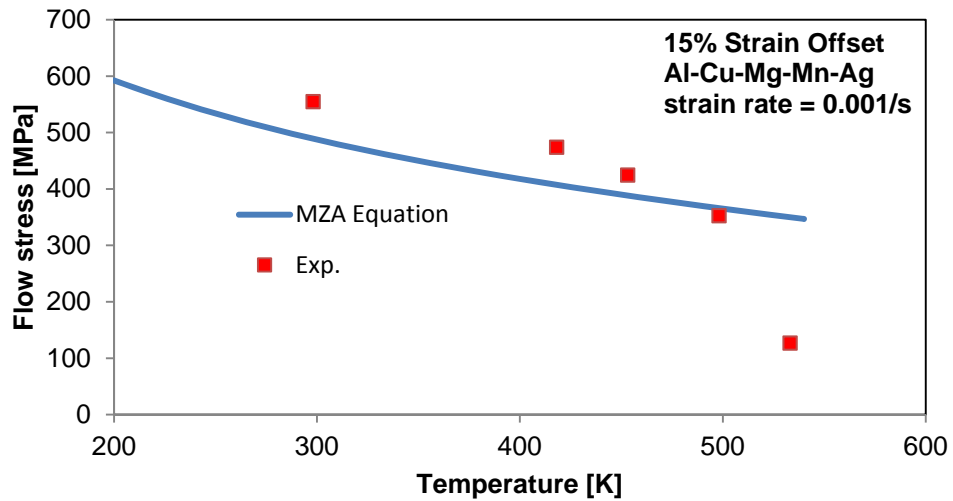


Figure 23. Thermal softening behavior of the flow stress for Al-Cu-Mg-Mn-Ag alloy: experimental data vs. prediction of modified Zerilli-Armstrong model.

Neither of the two physics-based material models (MTS and ZA models) takes into account the effect of the diffusion process on the threshold stress. With the help of the diffusion, dislocations can overcome the barriers by leaving their planes. Considering this, we propose the following modifications to ZA model and call it Turkkan-Vural modified Zerilli-Armstrong (TVZA):

$$\sigma = \sigma_a + \sigma^*$$

$$\sigma^* = 0.5\sigma_{th} \left[1 + \left(1 + \frac{4c_0\dot{\epsilon}T}{\sigma_{th}} \right)^{\frac{1}{2}} \right]$$

$$\sigma_{th} = \left[A(T) \left(1 + \sqrt{\left(\frac{1}{\omega} (1 - e^{-\omega\epsilon}) \right)} \right) \right] e^{-\alpha T}$$

where

$$\alpha = \alpha_0 - \alpha_1 \ln(\dot{\epsilon})$$

$$A(T) = A \left(1 - \left(\frac{T - T_0}{T_m - T_0} \right)^p \right)$$

After these modifications, TVZA model can finally capture the thermal softening behavior of complex Al-Cu alloys at high temperatures as shown in Fig. 24. Moreover, the $A(T)$ term in TVZA model can be modified to capture the desired thermal softening behavior observed in other different materials. Overall performance of TVZA model can be seen in Fig. 25 for a wide range of strain rates and temperatures.

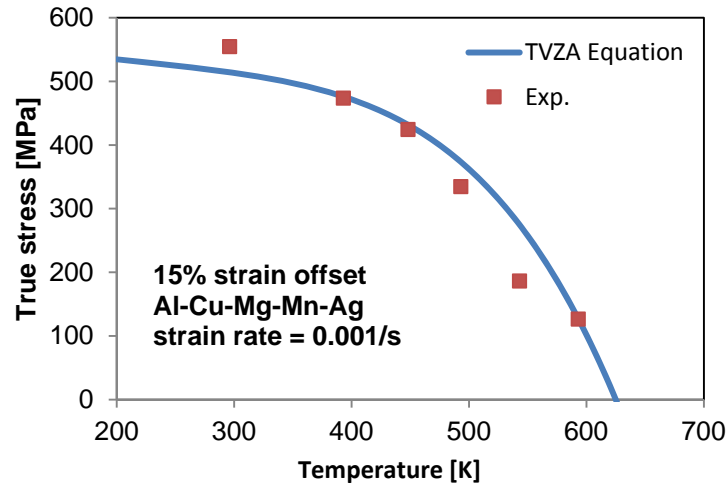


Figure 24. TVZA model can successfully capture the thermal softening behavior of the alloy even at elevated temperatures.

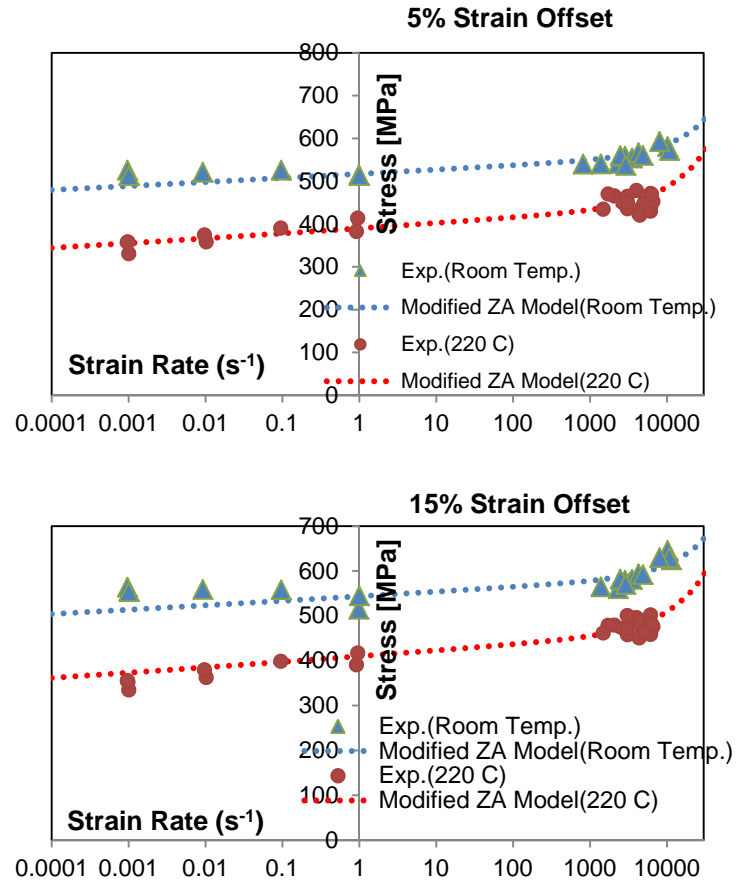


Figure 25. Al-Cu-Mg-Mn-Ag alloy modeled with proposed TVZA model, which shows increased strain-rate sensitivity in the dynamic regime.

(D) CONSTITUTIVE MODELLING WITH NEW TVZA MODEL:

Al-Cu, Al-Cu-Mg, and Al-Cu-Mg-Mn alloys have only room temperature data, but the rest of the materials have room temperature and elevated temperature experimental data in both quasi-static and dynamic strain rate regimes. Therefore, the following alloys which have the complete set of experimental data were modeled to test the performance of proposed constitutive models:

- [001] and [111] Single Crystals Al,
- Polycrystalline Al,
- Al-Cu alloy,
- Al-Cu-Mg-Mn-Ag alloy.

As discussed in the preceding section, original Zerilli-Armstrong (ZA) model excels in capturing less complex single-phase alloys such as Single Crystal Aluminum, Polycrystalline Aluminum and Al-0.1%Cu alloy. Therefore, these materials were modeled using the original ZA model with only increased rate sensitivity modification:

$$\begin{aligned}\sigma &= \sigma_a + \sigma^* \\ \sigma^* &= 0.5\sigma_{th} \left[1 + \left(1 + \frac{4c_0\dot{\epsilon}T}{\sigma_{th}} \right)^{\frac{1}{2}} \right] \\ \sigma_{th} &= B_0\epsilon^{\frac{1}{2}}e^{-\alpha T}\end{aligned}$$

where

$$\alpha = \alpha_0 - \alpha_1 \ln(\dot{\epsilon})$$

More complex Al-Cu-Mg-Mn-Ag alloy, on the other hand, was modeled using the Turkkan-Vural modified Zerilli-Armstrong (TVZA) model. Moreover, the listed alloys were also modeled using modified Johnson-Cook (MJC) model for the sake of completeness.

Single crystal aluminum has only room temperature data, and no further experiments were conducted at elevated temperatures. Therefore, it was modeled using only original ZA Model. Results presented in Figs. 26 and 27 show that the ZA model can successfully capture both the strain hardening and strain rate hardening of single crystal aluminum.

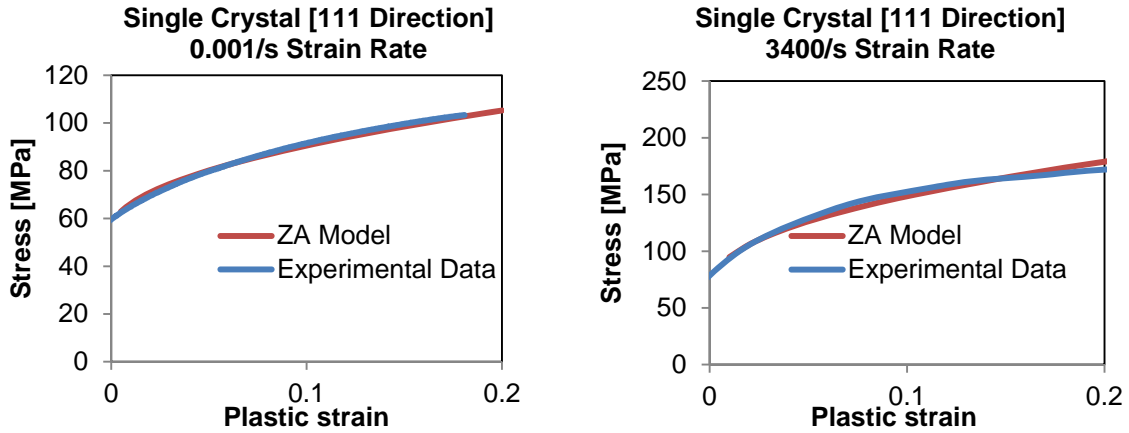


Figure 26. Single crystal [111] aluminum modeled with original ZA Model.

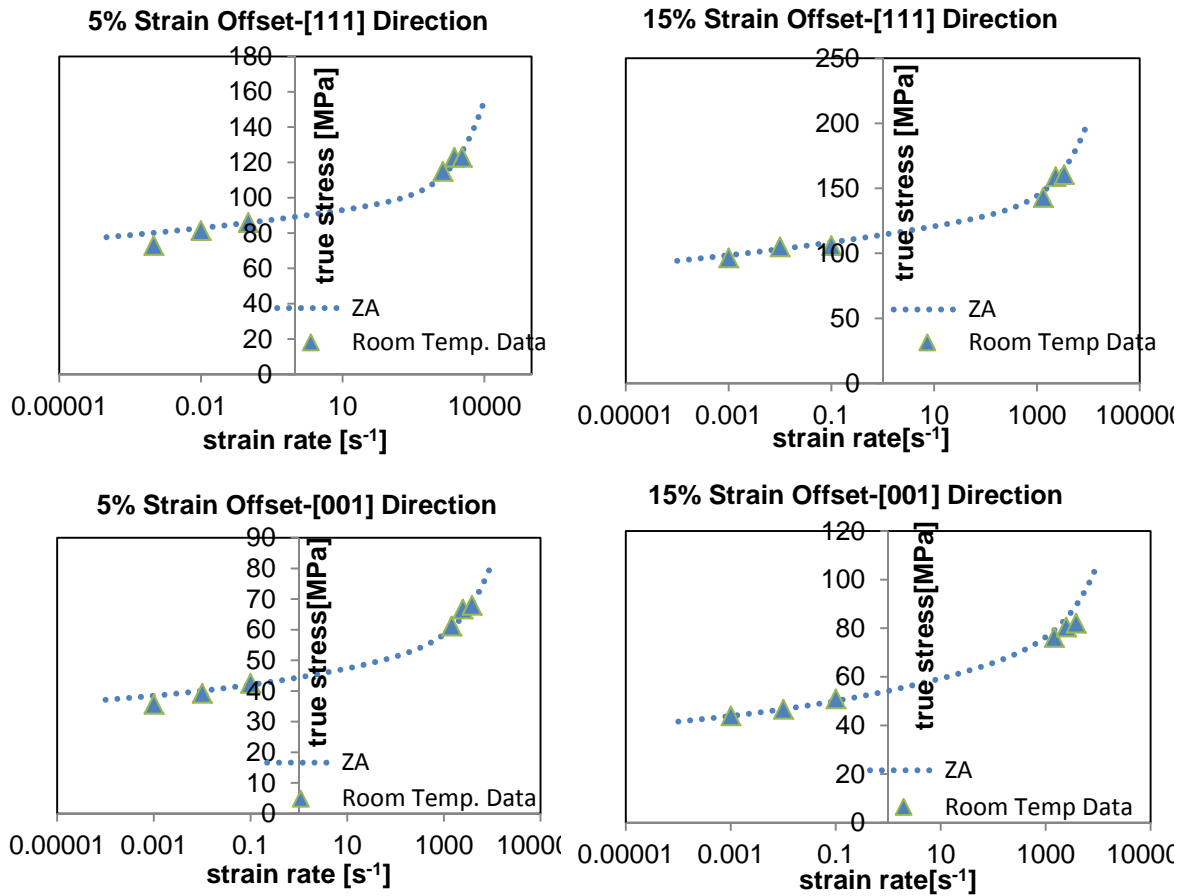


Figure 27. Single Crystal [111] and [001] aluminum modeled with original ZA Model.

Polycrystalline aluminum have the complete set of experimental data in both room temperature and elevated temperatures such as 120°C and 220°C. Modified Johnson-Cook (MJC) model and Zerilli-Armstrong (ZA) model were both used to predict experimentally observed flow stress as shown in Figs. 28 and 29, respectively.

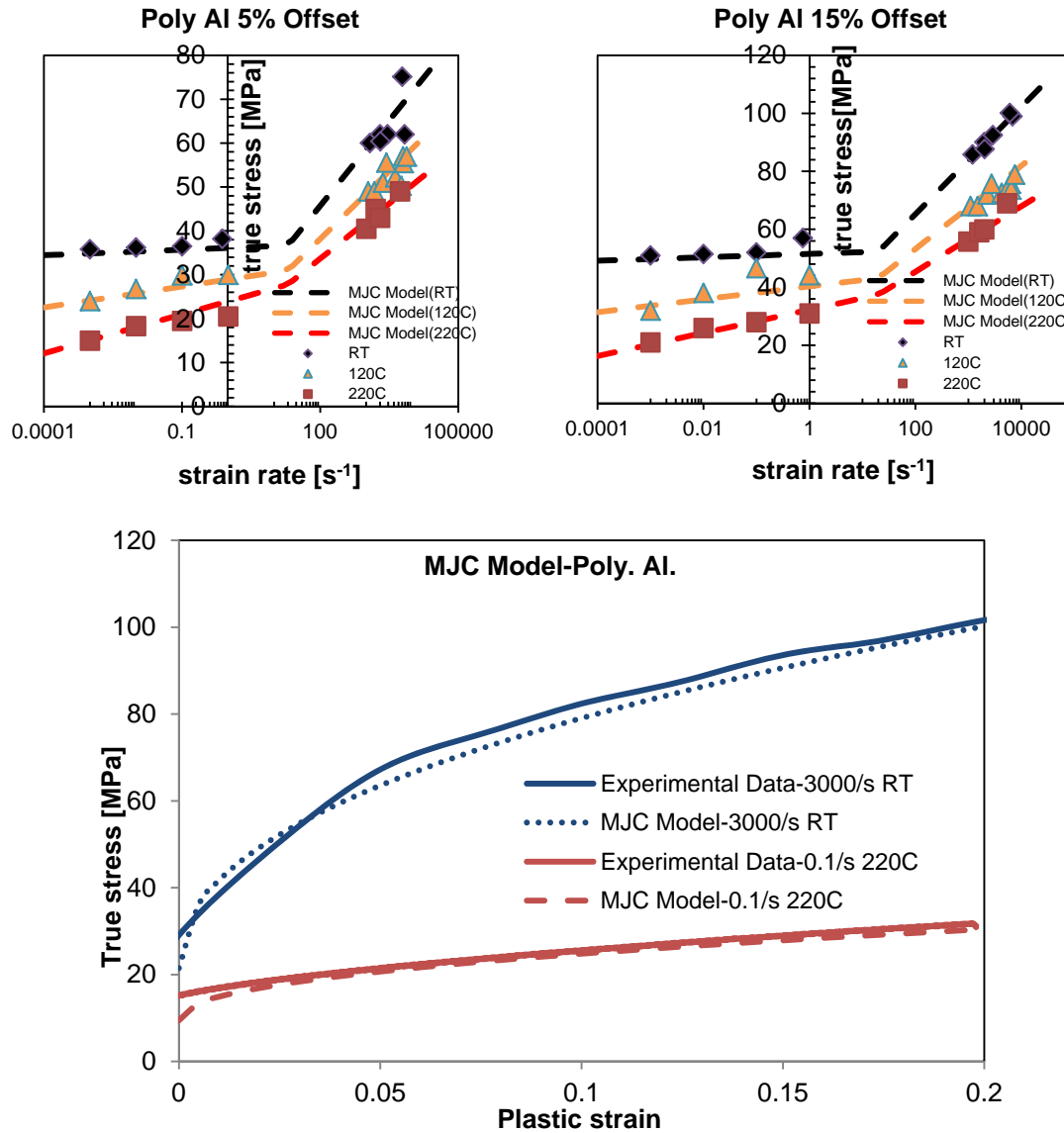


Figure 28. Polycrystalline aluminum modeled with MJC Model.

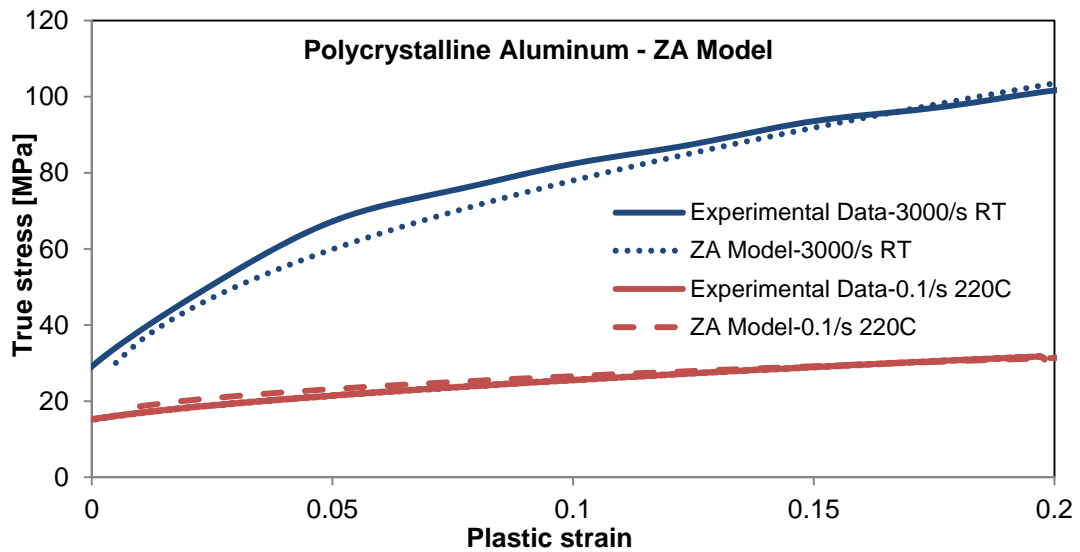
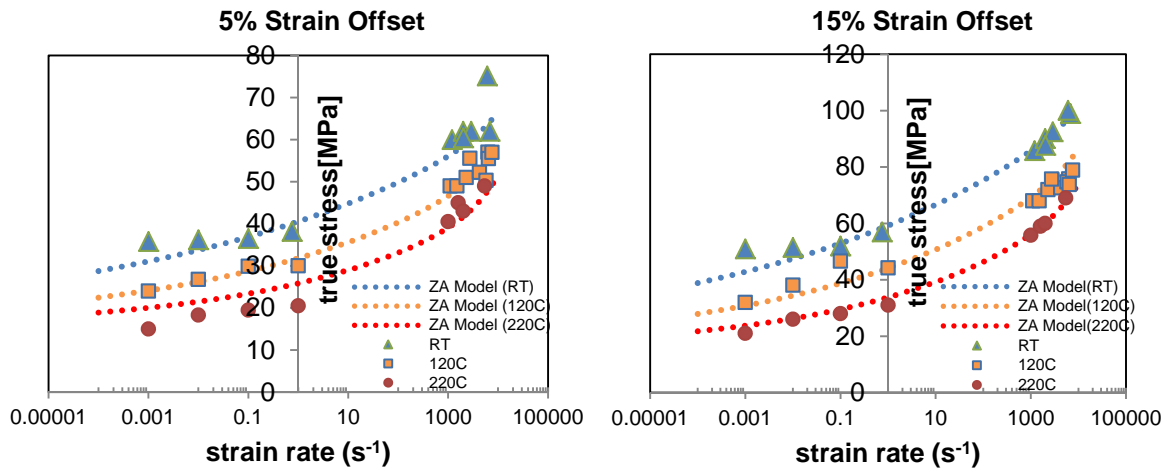


Figure 29. Polycrystalline aluminum modeled with ZA Model.

Al-0.1%Cu alloy has the complete set of experimental data in both room temperature and elevated temperatures such as 120°C and 220°C. Modified Johnson-Cook (MJC) model and Zerilli-Armstrong (ZA) model were both used to predict experimentally observed flow stress as shown in Figs. 30 and 31, respectively.

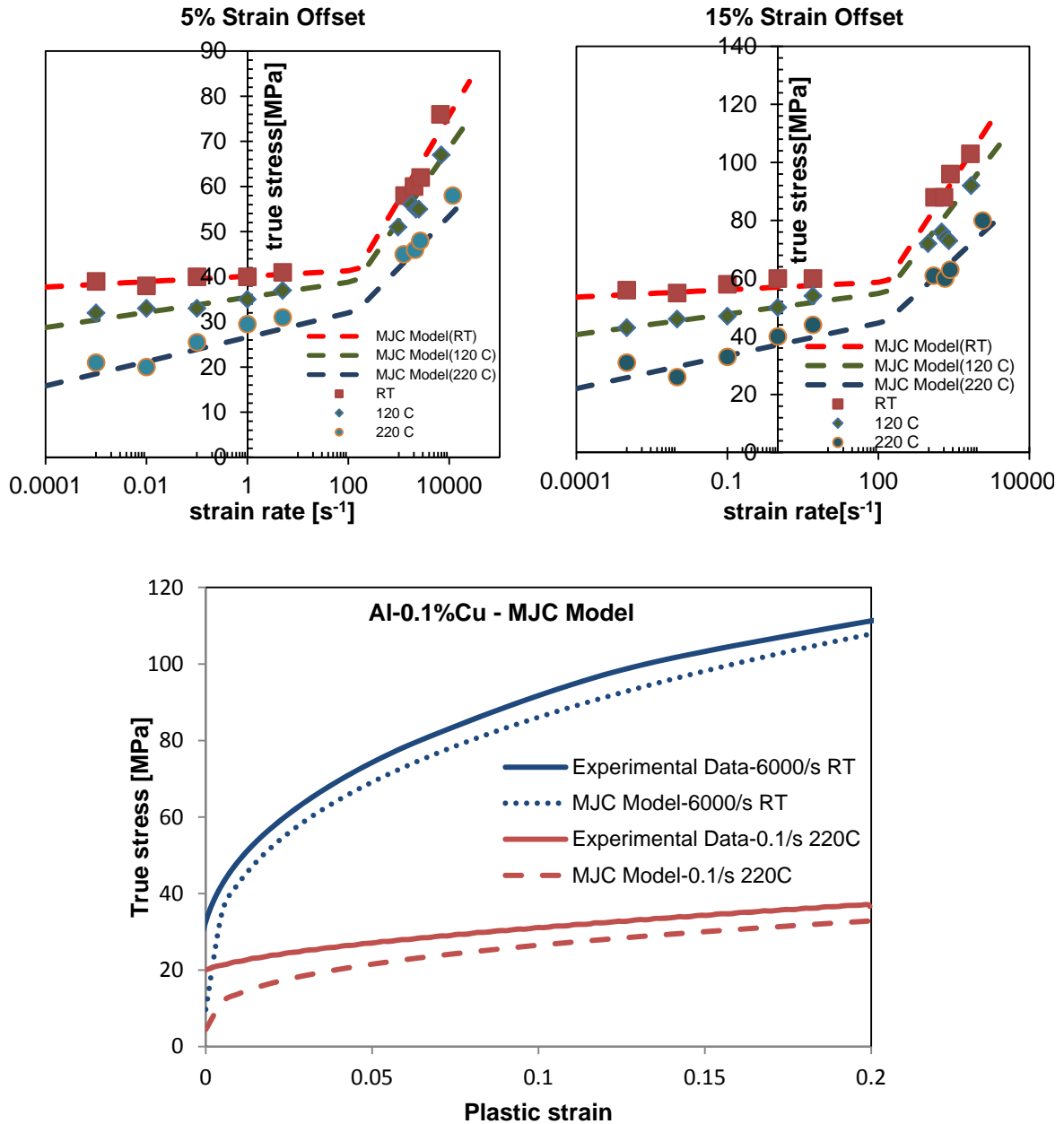


Figure 30. Al-0.1%Cu modeled with MJC model

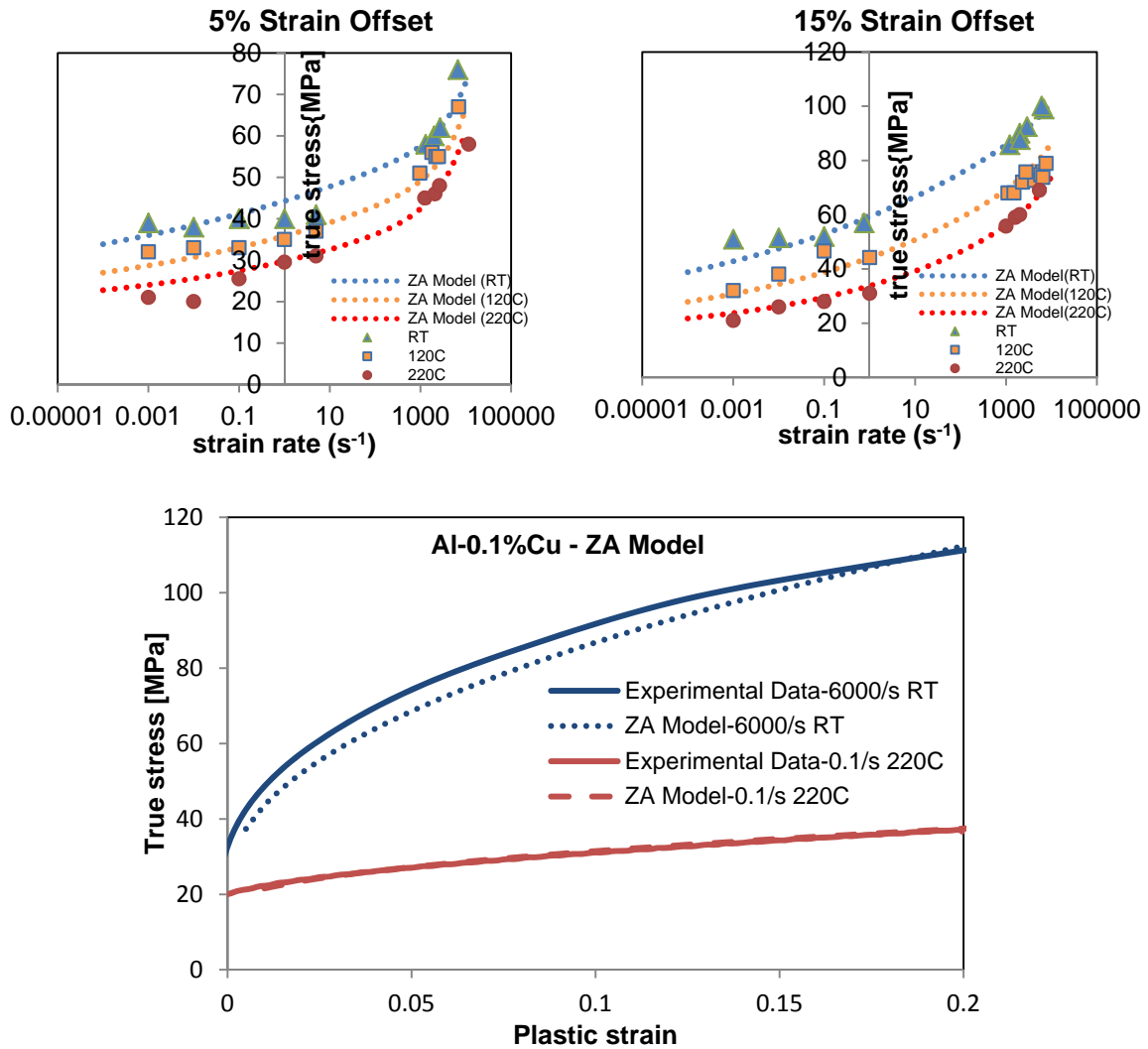


Figure 31. Al-0.1%Cu modeled with ZA Model.

Al-Cu-Mg-Mn-Ag alloy have complete set of experiments in room temperature, 120°C and 220°C. Also tests were done at elevated temperatures at a reference strain rate of 0.001/s. Modified Johnson-Cook (MJC) model and Zerilli-Armstrong (ZA) model were both used to predict experimentally observed flow stress as shown in Figs. 32 and 34, respectively. Figures 33 and 35 display the thermal softening behavior captured by the two models.

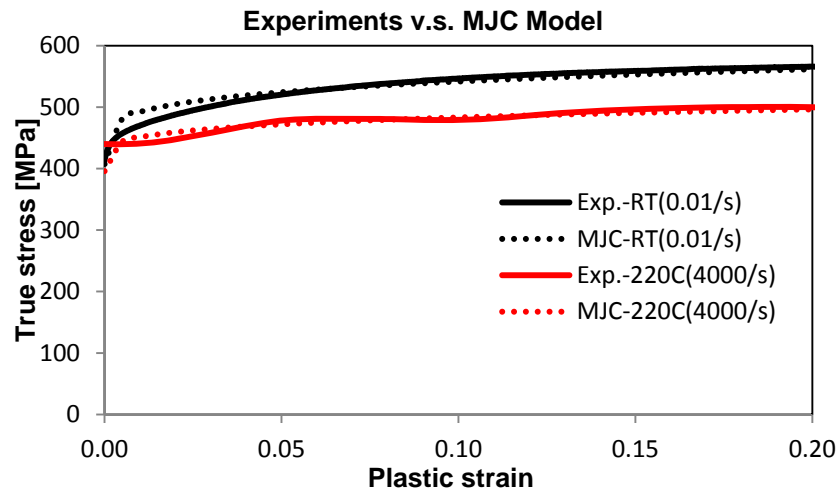
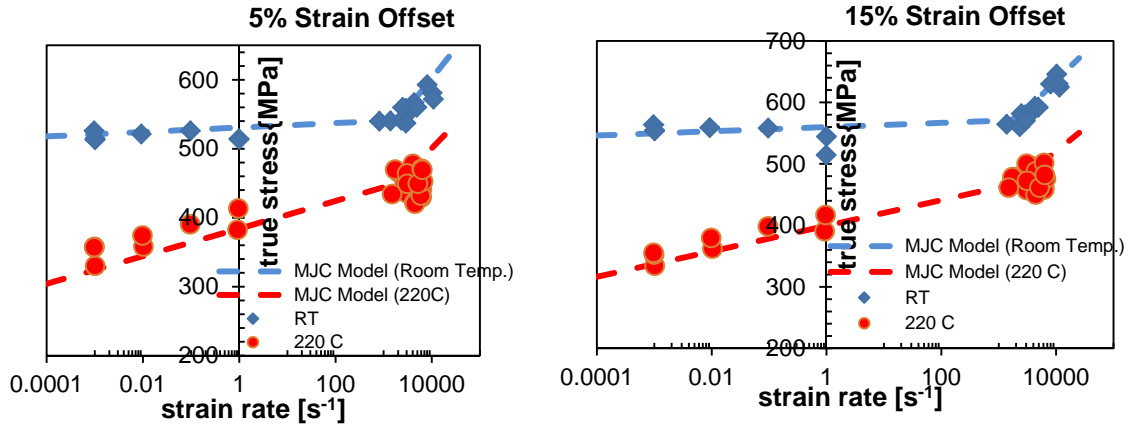


Figure 32. Al-Cu-Mg-Mn-Ag modeled with MJC Model.

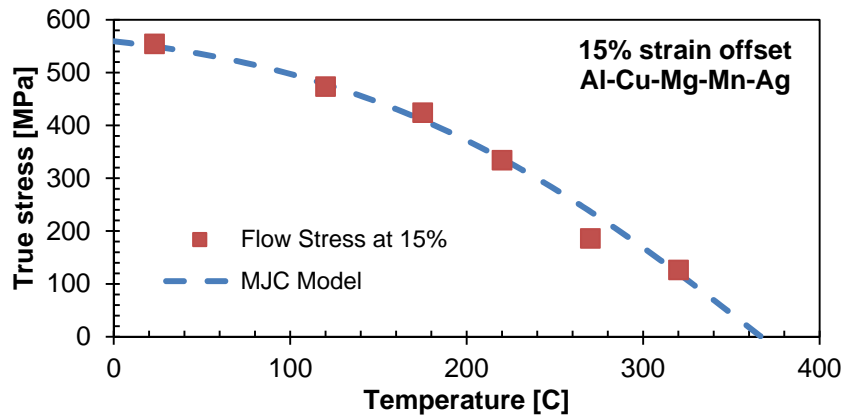


Figure 33. Thermal softening of Al-Cu-Mg-Mn-Ag alloy captured with MJC model, strain rate is 0.001/s.

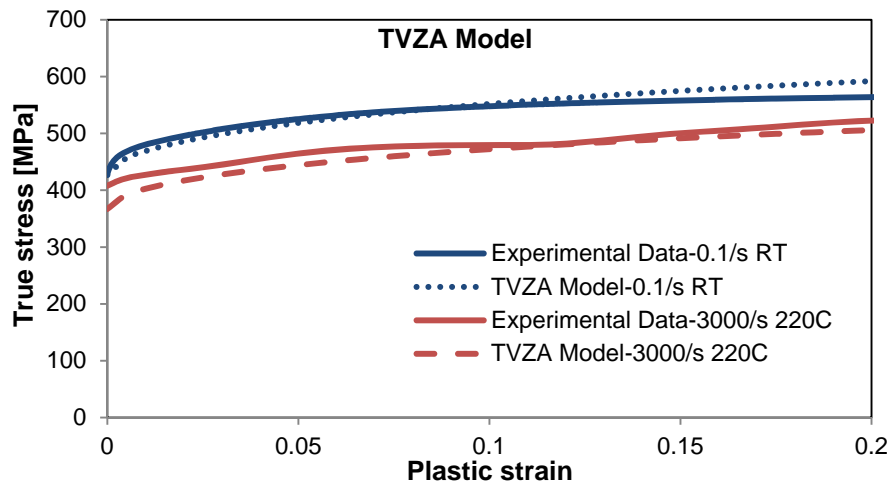
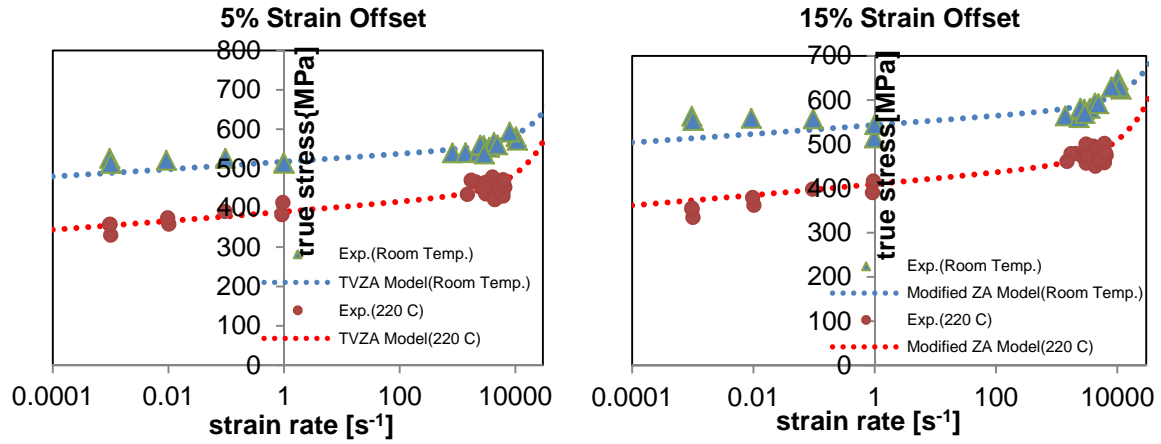


Figure 34. Al-Cu-Mg-Mn-Ag modeled with TVZA model.

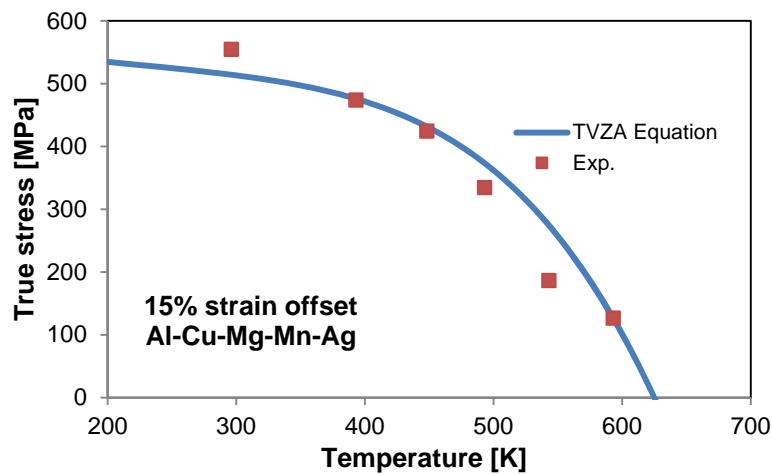


Figure 35. Thermal softening of Al-Cu-Mg-Mn-Ag alloy captured with TVZA model, strain rate is 0.001/s.

(E) ADIABATIC SHEAR BANDING:

In order to assess the propensity of various Al-Cu microstructures to failure by adiabatic shear banding, shear-compression specimens (SCS) were used in high strain rate SHPB experiments. Three alloys were tested using SHPB at nominally the same high strain rate of about 4000/s. High strain rate mechanical response of these SCS specimens are presented in Fig. 36 as equivalent plastic strain vs. equivalent true stress plots.

As can be observed from Fig. 36, the mechanical behavior of Al-Cu-Mg-Mn-Ag alloy processed in house is comparable to that of Al2139-T8 alloy, which has essentially the same chemical composition, both in terms of flow stress and the critical strain at which localized shear failure occurs. Flow stress exhibits a slight downward trend in both alloys in the strain range from 0.10 to 0.35/0.40, beyond which the onset of severe shear localization leads to adiabatic shear failure. On the other hand, Al-Cu-Mg-Mn alloy starts from a lower flow stress level of 380-400 MPa and show a significant strain hardening up until localized shear failure which occurs in a critical strain range of 0.45-0.50.

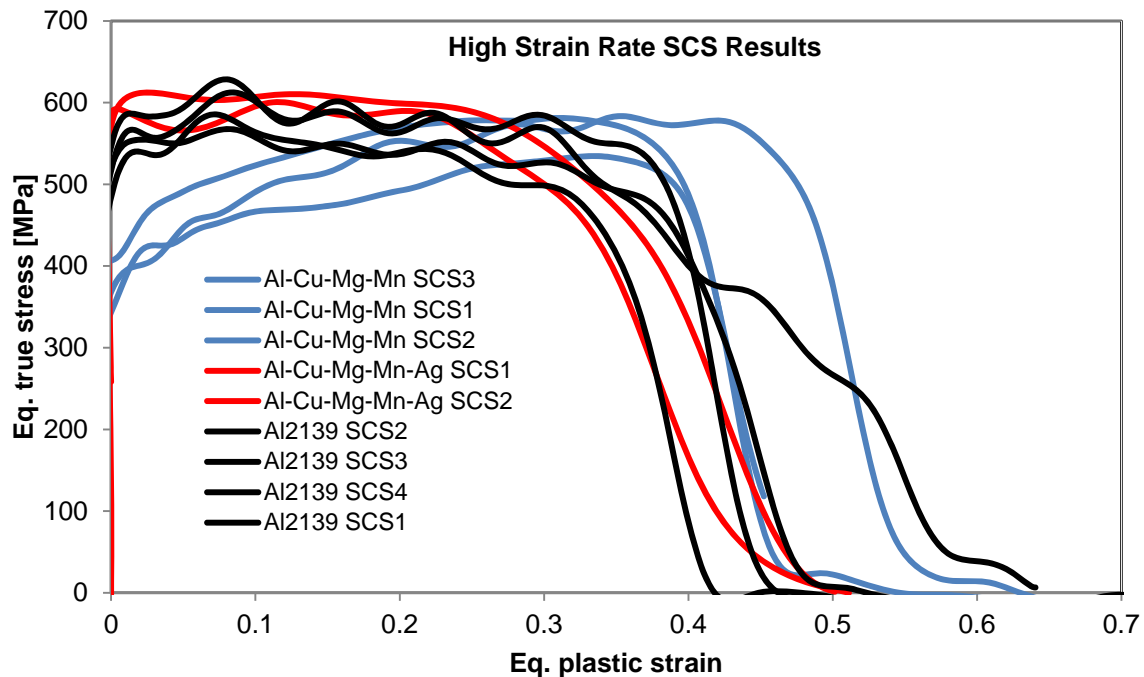


Figure 36. Shear-compression specimen (SCS) test results of three Al-Cu alloys. Strain rate is around 4000/s for all tests.

Considering the better ballistic performance of Al2139-T8 alloy, these macroscopic observations are a bit surprising. One would expect shear failure to occur at a larger critical strain in this alloy since delaying the onset of adiabatic shear localization is considered as one of the viable strategies in increasing the ballistic performance. From a purely macroscopic point of view, the only positive trait that justifies the higher ballistic performance of Al2139 alloy is the higher flow stress level. However, these macroscopic observations alone are not enough to assess the complete shear localization behaviour of

individual alloys. Therefore, we conducted Electron Backscatter Diffraction (EBSD) analysis using SEM to obtain a detailed characterization of the evolution of strains at microstructural scale as discussed in the following section.

(C) MICROSTRUCTURAL ANALYSIS OF DYNAMIC DEFORMATION:

Aluminum alloys, like many other metals, are susceptible to forming adiabatic shear bands (ASB) during high strain rate deformation, as opposed to the typical deformation response during static or quasi-static deformation. During high strain rate deformation, localized thermoplastic heating causes thermal softening and triggers the formation of ASBs that result in the accumulation of strain along narrow bands. The formation of ASBs is typically considered to be detrimental to the ballistic performance of materials and is often associated with the presence of geometrical or microstructural defects. Recent studies have reported that dynamic recrystallization (DRX) may precede and retard the formation of adiabatic shear bands, but others indicate that DRX requires more time to occur than is available during high strain rate deformation and could occur post-shear such as during the unloading process. To date, fundamental studies regarding the formation of adiabatic shear bands and how they may be controlled is still relatively limited, and further exploration may be required in order to fully understand the sequence of microstructural processes involved.

For this reason, Shear-compression specimens (SCS) have been subjected to controlled high strain rate loading histories up until prescribed equivalent strains in a split Hopkinson pressure bar (SHPB) setup by using stop rings of various sizes. Then, post-mortem EBSD analysis of recovered specimens was performed to elucidate the effects of the grain orientations, secondary phases, and precipitates on the development and evolution of adiabatic shear bands in three distinct alloy compositions: (1) Al-Cu, (2) Al-Cu-Mn-Mg, and (3) Al 2139 alloy. EBSD mapping was used to reveal the Schmid Factor associated with different grain orientations, indicating which grains experienced higher or lower resolved shear stresses during deformation. Quantification of the dominant deformation mechanisms as a function of alloy composition and microstructure was performed to provide scientific insight on how to better engineer and optimize the properties of aluminum alloys for high strain rate applications. The composition of these alloys are shown in Table 4 by percent weight. Multiple shear-compression specimens were machined from each of the alloy compositions and microstructural changes in the material were quantified as a function of equivalent strain.

Table 4: Major alloying elements of the systems investigated. Listed values reflect the weight percent of the respective element in the system.

	<i>Al-Cu</i>	<i>Al-Cu-Mn-Mg</i>	<i>AA 2139</i>
<i>Cu</i>	4.5	4.5	4.5-5.5
<i>Mn</i>	-	0.3	0.20-0.6
<i>Mg</i>	-	0.5	0.20-0.8
<i>Ag</i>	-	-	0.15-0.6

The model Al-Cu and Al-Cu-Mn-Mg alloys were processed in the laboratory as ~600g heats. High purity, elemental additions were induction melted in a high purity alumina crucible under an inert cover gas and cast into a steel mold to produce bars measuring 39 mm by 25 mm (cross section) and 80 mm long. After casting, the materials were subjected to a homogenization heat treatment at a temperature between 803-808 K (530-535 °C) for 3-5 hours to minimize dendritic segregation in the cast structure. Following, the bars were hot rolled just above their respective solvus temperatures (the same used for homogenization) until the plates were reduced to ~10 mm in thickness in order to break up the cast structure and refine the grain size. Recrystallization was then induced via annealing just above the solvus temperature. After quenching, the bars were immediately placed into an aging furnace and aged such that peak hardness was achieved. Afterwards, the shear-compression specimens were extracted from these aged plates. The 2139 shear-compression specimens were extracted directly from a ~50mm thick cold rolled plate that was aged to peak hardness.

Samples were extracted such that the rolling direction was aligned along the length of the sample. Both sets of shear-compression specimens had a cylindrical shape with diameter, D , 6.35 mm and length, L , 12.7 mm. Angled slots of a width, w_o , of 1.27 mm were machined symmetrically on both sides of the sample at a 35.3 degree angle, α , relative to the base of the sample and such that they were centered relative to the sample's height, Figure 37. The applied axial stress, P , to the sample would then be translated to shear stress upon compression and localized to the area within the machined slots. The remaining sample thickness within the slotted area, t_o , after machining was approximately 1.59 mm.

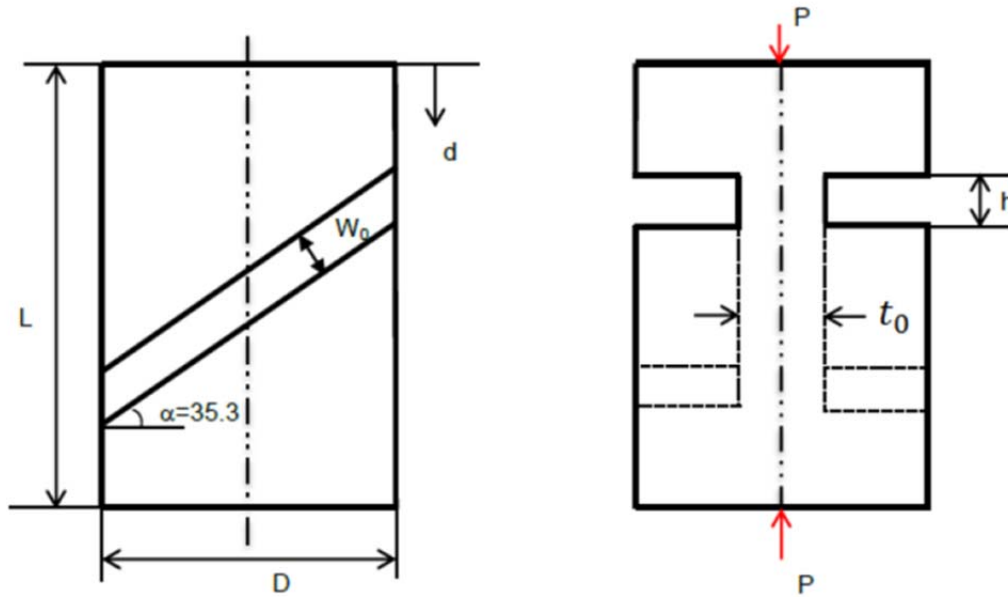


Figure 37. Shear-compression specimen (SCS) geometry used in SHPB tests.

After compression to the specified strain levels, samples were sectioned in half longitudinally and parallel to the previously machined slots such that the entire height of the sample could be metallographically prepared for EBSD characterization. Samples were prepared using standard metallographic techniques and a final polish of 0.06 micron colloidal silica suspension. EBSD characterization of the samples was completed using a JEOL-5900 LV SEM equipped with an Oxford Nordlys-HKL EBSD detector. Micro-Vickers hardness indents were used as fiducial markers such that large area mapping could be completed accurately. EBSD scans were conducted along the height of the sample, capturing the entire slot region and surrounding bulk material. Maps were stitched together and analyzed using the Oxford HKL Channel 5 software package. After conservative noise reduction was performed, inverse pole figure and local misorientation maps were prepared for analysis and interpretation. Additionally, both texture and Schmid factor analysis was performed in order to observe any possible tendencies the shear banding might have with respect to specific crystallographic orientations relative to the loading direction. Precipitate characterization was completed using a Phenom ProX benchtop SEM. Backscattered electron images with elemental contrast were collected and the precipitation was quantified using the ImageJ software.

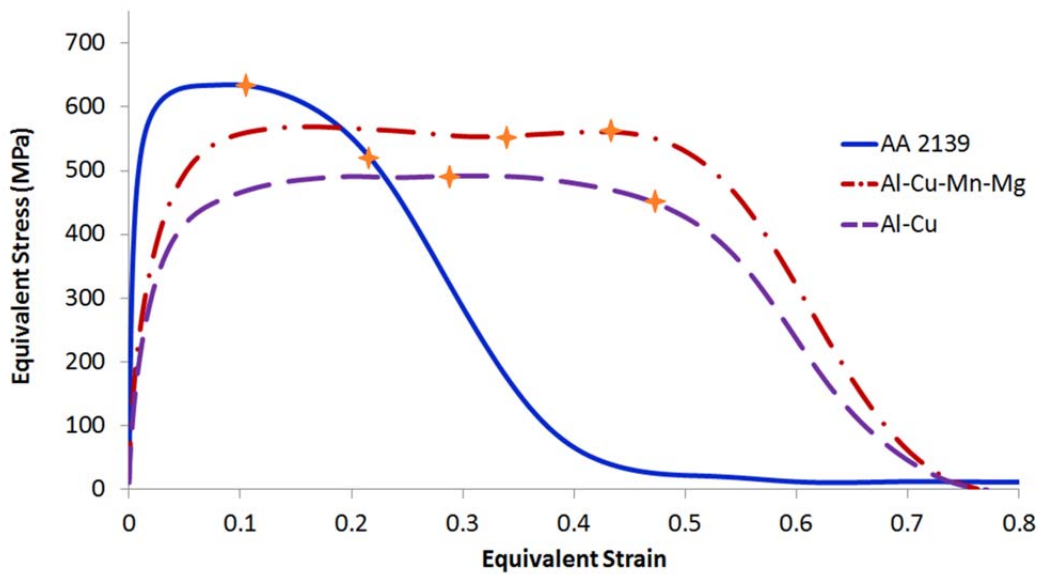


Figure 38. Shear localization curves for the alloys investigated for EBSD analysis. Controlled dynamic tests are indicated on the plots. Strain rate is about $12,000 \text{ s}^{-1}$ in all experiments

Equivalent stress-strain curves for the SCSs in all of the alloy systems demonstrated strain softening behaviors after the ultimate stress was reached, until finally arriving at a critical strain where the mechanical properties of the alloy became significantly degraded (see Fig. 38). One must note that the shear localization curves presented in Fig. 38 is quite different from those in Fig. 36 because of the different slot width (w_o) and strain rates involved. Specimens used for EBSD analysis had half the slot width of those used in initial SCS experiments, and the strain rates were three times higher. Critical strain for each of the three alloys was systematically determined by the intersection of the slopes of the strain softening behavior and the sharp downward flow stress that signified failure.

The rapid degradation of the material's ability to accommodate stress can likely be attributed to localized shear failure within the microstructure. For example, in the Al-Cu alloy, the onset of strain softening was observed to occur after an equivalent plastic strain of 0.35 was reached, and the subsequent flow properties were seen to rapidly degrade after a strain of 0.49 was reached. For comparison, onset of strain softening in the Al-Cu-Mn-Mg alloy and 2139 occurred following an equivalent strain of 0.51 and 0.22, respectively. The strain softening behavior is more pronounced in the 2139 specimen, where shear failure appears to occur relatively more slowly. Points at which interrupted tests were conducted are indicated along the stress-strain curves in Fig. 38.

Low magnification, stitched EBSD maps were conservatively post processed such that several different map types could help reveal the microstructural effects present in the material as a function of room temperature, high strain rate deformation. Prior to deformation, as the Al-Cu and Al-Cu-Mn-Mg alloys were fully recrystallized, no noticeable crystallographic texture was observed. For the Al-Cu alloy, the mean grain size within the slotted gage section was approximately 670 while the Al-Cu-Mn-Mg alloy had a mean grain size of approximately 85 microns. In the case of 2139, the mean grain size was measured to be approximately 175 microns. Inverse pole figure maps shown in Fig. 39 show the changes occurring in the microstructure and crystallographic orientation as a function of equivalent strain. Referring to Figs. 39e and f that correspond to the microstructure of 2139, a significant increase in intragranular misorientation was observed as the equivalent strain increased from 0.11 to 0.22. A significant increase in the degree of grain rotation along the edge of the machined slot, where the stress concentration was the highest, was also observed. Increases in intragranular misorientation and grain rotation between strain levels were also observed in the other two alloy systems investigated.

To most effectively quantify the ability of the microstructures to accumulate deformation, local misorientation maps were generated using the Channel 5 software package for EBSD post processing. Local misorientation maps were created using a 3x3 filter such that local deviations could be readily detected. Subgrain boundaries were defined as having <5 degree boundaries and any local misorientations exceeding this were not averaged. The extent of local misorientation was observed to increase as a function of equivalent strain for all samples. However, the level of local misorientation was observed to be higher in samples containing more alloying elements (see Fig. 40). By integrating and averaging the relative local misorientation profiles over the slotted "gage" section of the sample, where the shear-compression deformation is actually occurring, it was found that the Al-Cu samples' local misorientation increased from approximately 0.9 degrees/mm² to approximately 1.1 degrees/mm² between the equivalent strain levels of 0.34 and 0.42. Likewise, for the Al-Cu-Mn-Mg samples, the average local misorientation increased from approximately 1.5 degrees/mm² to approximately 1.8 degrees/mm² between the axial strain levels of 0.30 and 0.47. Finally, the 2139 samples experienced a local misorientation increase from approximately 1.7 degrees/mm² to approximately 2.0 degrees/mm² between the axial strains of 0.11 and 0.22.

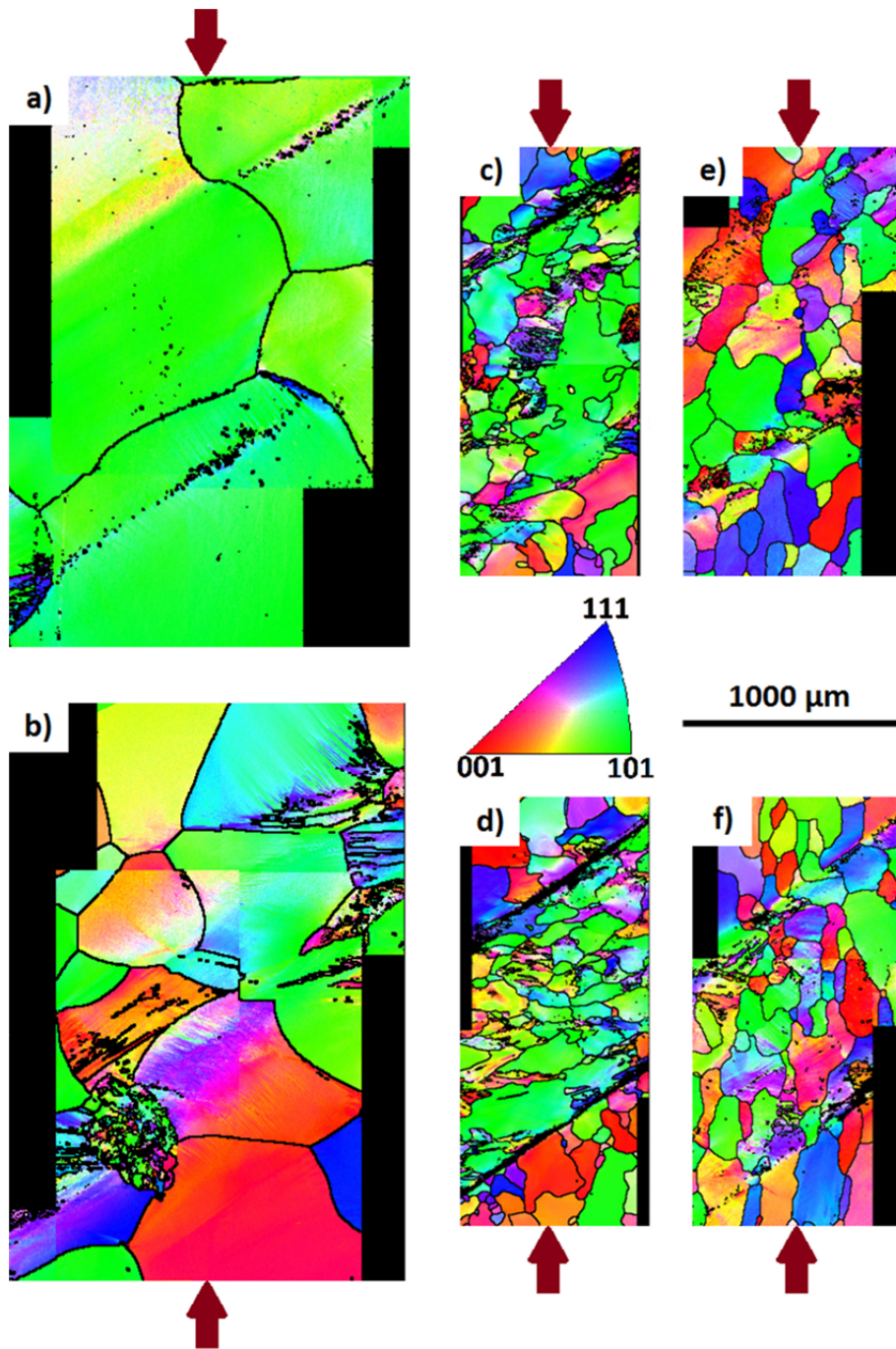


Figure 39: Inverse pole figure maps for the slotted “gage” sections for the series of alloys. Orientations are shown with respect to the loading direction. Loading direction indicated with arrows. a) Al-Cu after an equivalent plastic strain of 0.34, b) Al-Cu after an equivalent strain of 0.42, c) Al-Cu-Mn-Mg after an equivalent strain of 0.30, d) Al-Cu-Mn-Mg after an equivalent strain of 0.47, e) 2139 after an equivalent strain of 0.11, and f) 2139 after an equivalent strain of 0.22.

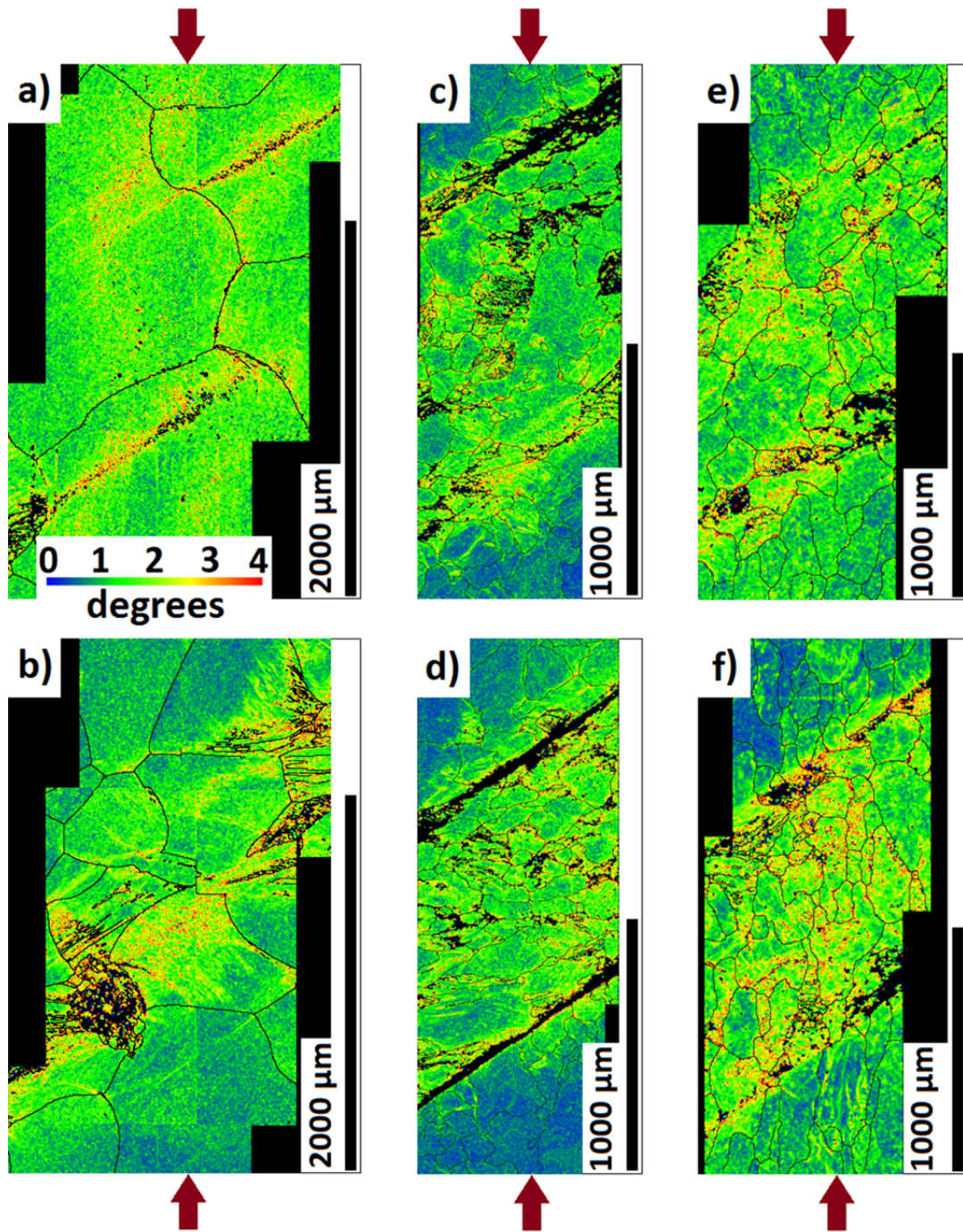


Figure 40: Local misorientation maps for the slotted “gage” sections of: a) the Al-Cu sample deformed to an equivalent strain of 0.34, b) the Al-Cu sample deformed to an axial strain of 0.42, c) the Al-Cu-Mn-Mg sample deformed to an axial strain of 0.30, d) the Al-Cu-Mn-Mg sample deformed to an axial strain of 0.47, e) the 2139 sample deformed to an axial strain of 0.11, and f) the 2139 sample deformed to an axial strain of 0.22. The higher strain values are proportionally equivalent between samples, relative to their respective critical strain values. Loading direction indicated with arrows.

Shear band formation was observed in all three alloy systems at high strain levels, following the formation of large shear-like bands at the lower strains. Higher magnification EBSD maps revealed that the shear bands in all of the alloys had a tendency to become more defined as deformation progressed. For example, in the Al-Cu samples, it was observed that the relative boundary misorientation between the shear bands increased from 20 degrees, on average, after an axial strain of 0.34, to 40-45 degrees after becoming more defined at an effective strain of 0.42 (see Fig. 41). For the Al-Cu-Mn-Mg sample with an effective strain of 0.30, the boundaries ranged in misorientation from 20-35 degrees with an average of 30 degrees, increasing to a range of 35-45 degrees with an average of 30 degrees after reaching an axial strain of 0.47. With respect to the 2139 alloy, a range of 15-35 degrees was observed after axial compression to a strain of 0.11, increasing marginally to a range of 15-40 degrees with an average of 25 degrees after an additional strain to 0.22.

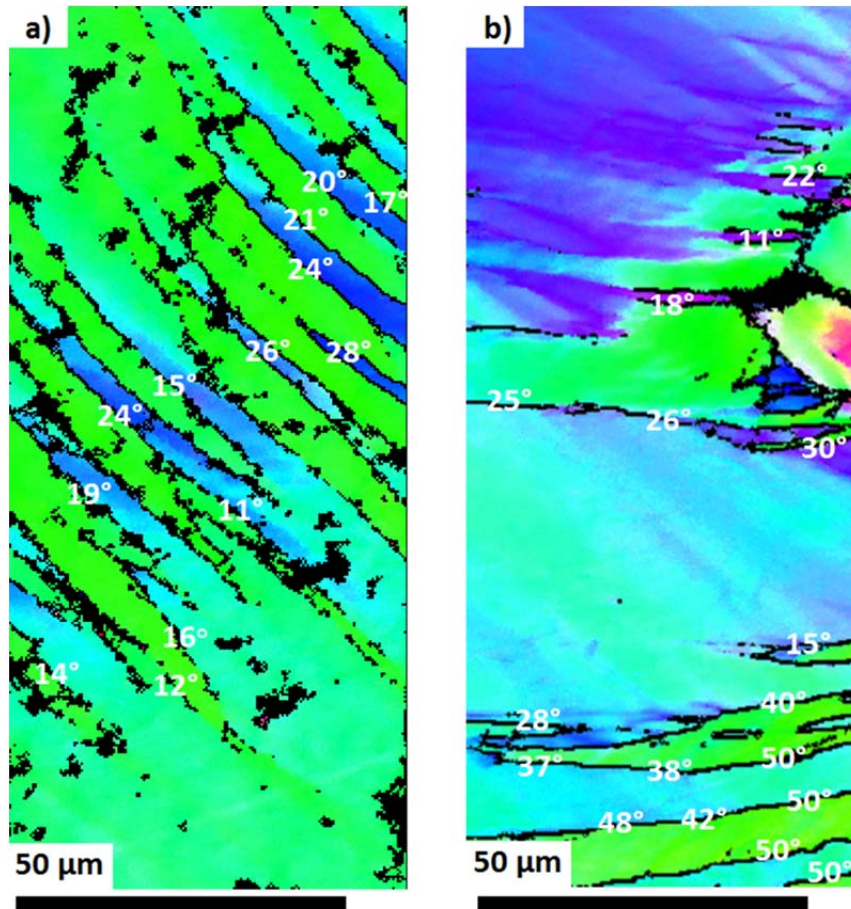


Figure 41: Shear bands observed in Al-Cu samples after a) an equivalent strain of 0.34, and b) an equivalent strain of 0.42. Relative boundary misorientation is shown at the boundaries in the images.

To better understand the effects of crystallographic orientation on the formation of shear bands, texture maps were generated such that the orientations of interest, relative to

the axis of compressive loading, were highlighted. It was observed in all samples that the formation of shear bands was noticeably absent along the $\{111\}$ and $\{100\}$ planes. Rather, when shear bands were present, they exhibited a tendency to form close to a number of other crystallographic planes. For example, in the 2139 system the planes near which they were observed to form included $\{101\}$, $\{103\}$, $\{210\}$, $\{211\}$, $\{221\}$, and $\{314\}$. Figure 42 shows the slip activity along the $\{101\}$, $\{103\}$, $\{211\}$, and $\{314\}$ planes, which were the most pronounced. However, texture maps also indicated that over the length of all of the specimens, few grains were oriented such that their $\{111\}$ or $\{100\}$ planes were aligned with the direction of axial loading. Therefore, no functional trends were revealed from these texture maps regarding any preferential formation of shear bands along specific planes.

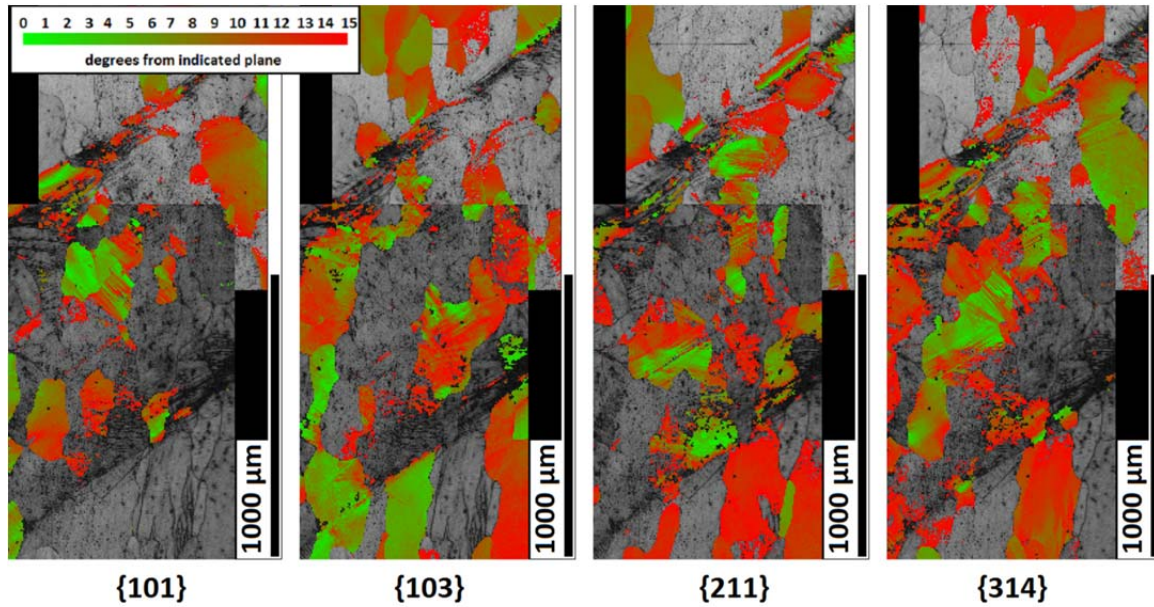


Figure 42: Band contrast texture maps for the 2139 sample after 0.22 equivalent plastic strain, highlighting which portions of the microstructure has designated crystallographic planes in alignment with loading direction. In highlighted portions the loading direction is within 15 degrees of the indicated plane according to the gradient legend shown. Green regions are in alignment with the loading direction. Red regions are 15 degrees away from being aligned with the loading direction. Regions not highlighted are more than 15 degrees away from the loading direction.

EBSD post processing also allowed for the mapping of the Schmid factor with respect to the loading direction. Schmid factor maps revealed that the slip directions in $\{111\}$ planes typically had a Schmid factor of approximately 0.35 before they were exposed to stress, indicating that they would only be subjected to 70% of the resolved shear stress that those grains with the highest possible Schmid factors of 0.5 would be absorbing in other crystallographic orientations. For all cases, maps also revealed that within the slotted “gage” section of the shear-compression specimens, Schmid factors rose in correlation with increasing deformation indicating that higher resolved shear stresses would then be present in the gage section. For example, in the Al-Cu-Mn-Mg

alloy, Fig. 43, it can be seen that the Schmid factor distribution inside the slotted “gage” section shifts in favor of higher Schmid factors as the equivalent strain increases.

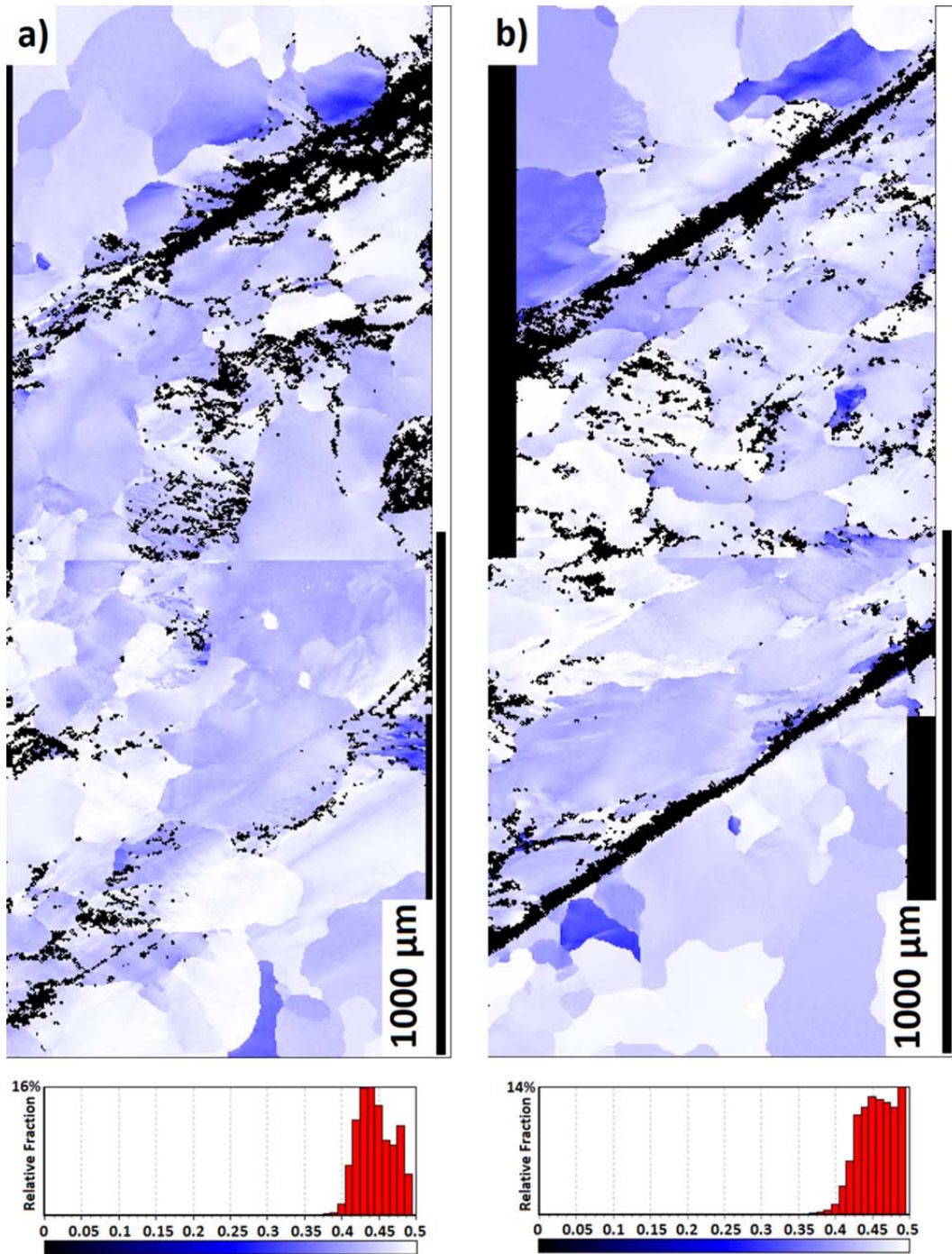


Figure 43: Schmid factor maps and histograms for the Al-Cu-Mn-Mg system at the equivalent plastic strain levels of a) 0.30 and b) 0.47. Histograms for the center slotted “gage” section shift towards the right, indicating higher Schmid factors and therefore higher resolved shear stresses would be present as deformation progresses.

Precipitates within the microstructures of all alloys were characterized using backscattered electron imaging to produce elemental contrast. Characterization of the alloys confirmed the presence of both intragranular precipitates within the grains and along the grain boundaries as shown in Fig. 44. The fraction and distribution of precipitates observed within the microstructure was proportional to the degree of alloying additions in the material with the least observed in Al-Cu and the most observed in 2139. In 2139, the larger precipitates (~3-5 microns in size) were confirmed to be of the Al_2Cu composition, which corresponds to the omega precipitate. In the Al-Cu samples, the area fraction of precipitates was measured to be approximately 0.2%. The addition of 0.3wt.% Mn and 0.5wt.% Mg in the Al-Cu-Mn-Mg samples increased the area fraction of precipitates to approximately 1.1%. With nominally similar alloying levels of Cu, Mn and Mg, the addition of Ag in the 2139 samples served to slightly increase the area fraction of precipitates to approximately 1.2%. Averages were taken over several images in different areas of the sample to ensure that the values were statistically significant. Precipitate sizes ranged from approximately 100 nanometers in diameter up to 2-5 microns in diameter. The average size of these precipitates was also observed to marginally decrease with the addition of more alloying elements, starting with a Feret diameter of approximately 0.80 microns in the Al-Cu system and decreasing to approximately 0.73 microns in the Al-Cu-Mn-Mg system, and finally to approximately 0.69 microns in the 2139 alloy.

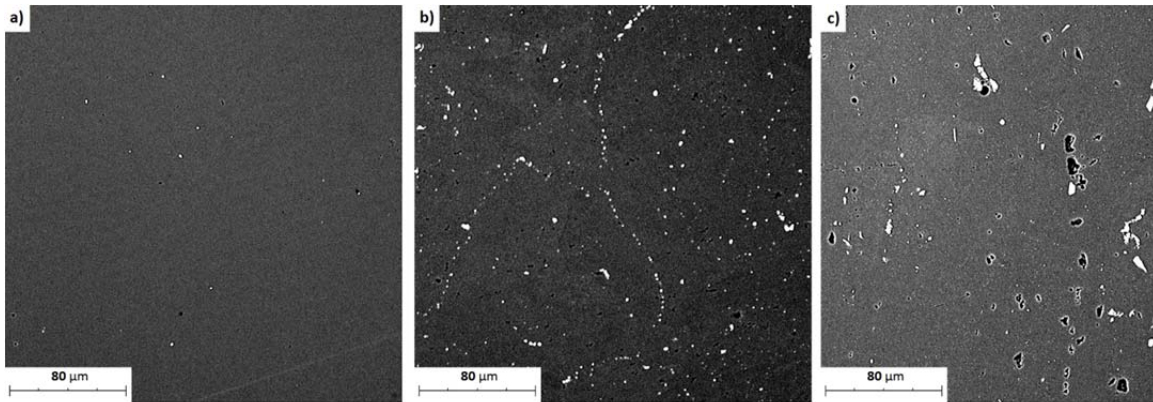


Figure 9: Al_2Cu precipitates present in a) the Al-Cu alloy, b) the Al-Cu-Mn-Mg alloy, and c) the 2139 alloy. Note that the area fraction of precipitates increases as alloying elements are added. Image C shows a wider range of precipitate sizes; many precipitates are very fine at this magnification.

Figure 44: Al_2Cu precipitates present in a) the Al-Cu alloy, b) the Al-Cu-Mn-Mg alloy, and c) the 2139 alloy. Note that the area fraction of precipitates increases as alloying elements are added. Image C shows a wider range of precipitate sizes; many precipitates are very fine at this magnification.

(G) DISCUSSION AND CONCLUSIONS:

As expected, increasing the level of alloying in these Al alloys contributed to the enhancement of strength in the material, as was evidenced in the high-strain-rate stress strain curves in this study. Increases in precipitation resulted in a higher degree of strengthening and an increase in the peak stress that was measured to be 500 MPa, 570MPa and 630MPa for the the Al-Cu, Al-Cu-Mn-Mg, and 2139 system, respectively.

Interestingly, despite the higher flow stress behavior for the Al-Cu-Mn-Mg alloy, the magnitude of effective strain achieved before shear failure was approximately the same as that for the Al-Cu alloy. For 2139, however, the critical strain was reduced to approximately 0.22. Characterization of the samples after dynamic deformation revealed that the degradation of the mechanical properties and flow softening behavior of the alloys could be attributed to the formation of shear bands within the microstructure. The onset of this rapid degradation was characterized by a critical strain value that was detected in the equivalent stress strain curve.

EBSD inverse pole figure maps revealed that a heterogeneous strain distribution was largely accommodated by the microstructure along the edges of the slotted “gage” section of the samples, Figure 39. Within these regions, particularly in the Al-Cu specimens, some grains were able to complete a full rotation between the $\{111\}$ and the $\{101\}$ planes with respect to the sample normal direction. Sub-grain structures were observed within the highly deformed grains. As strain levels increased, these select grains were observed to show signs of refinement or recrystallization as discrete grain structures were formed. Inverse pole figure maps also confirmed the presence of shear band formation within this section of the microstructure. Quantification of the progression of shear band formation in all of the alloys as a function of effective strain revealed that the boundaries formed by these bands experienced a significant increase in boundary misorientation as the magnitude of plastic deformation increased. As such, bands which were more completely formed would be allowed to flow more freely, decreasing the required applied stress to continue plastic flow.

For all three alloys, texture analysis revealed that shear banding was noticeably absent along the $\{111\}$ and $\{100\}$ planes. Analysis of the Schmid factors associated with grains within the gage section of the each of the shear – compression specimens revealed that the $\{111\}$ planes typically had a Schmid factor of approximately 0.35. For the shear-compression specimens, it was assumed that the gage section of the sample was subject to a uniaxial state of stress; friction was negligible and plastic flow was confined to the gage section. Thus, for the given loading direction and a peak stress level of 630 MPa, the maximum resolved shear stress translated to the slip directions in $\{111\}$ planes would only be 220.5 MPa out of a possible 315 MPa. Based on this analysis, grains orientated with Schmid factors approaching 0.5 would be more susceptible to form shear bands first. As deformation progressed, granular rotation and texturing occurred such that more of the microstructure became aligned in favor of a higher Schmid factor, and therefore higher, more evenly distributed resolved shear stresses. This increased the probability of more homogeneous and more rapid formation of shear bands.

Based on the observations from this study, the ability of these Al alloys to accumulate deformation within the microstructure prior to the rapid degradation of the mechanical properties via shear banding was closely associated with the presence of precipitates in the microstructure. Increases in the area fraction of precipitates within the microstructure as a function of the addition of alloying elements, as well as the slight decrease in average Feret diameter of those precipitates, caused the alloys to accumulate higher levels of local misorientation within the grains as the deformation progressed. At effective strain levels approaching the critical strain level for rapid degradation of mechanical properties, the microstructure of 2139 exhibited an average local

misorientation of 2.0 degrees over a square millimeter area. Whereas Al-Cu and Al-Cu-Mn-Mg samples, which were found to contain lower area fractions of precipitates, the average local misorientations were measured to be 1.1 and 1.8 degrees, respectively.

During plastic deformation, precipitates serve to pin dislocations along the precipitate – matrix interface. Since dislocation climb processes are limited during high strain rate deformation, in order for planar slip to occur, the magnitude of the resolved shear stresses acting on the dislocation must exceed those associated with precipitate shearing or looping. Grain rotations during deformation are largely associated with planar slip conditions. In the Al-Cu specimens, the comparatively low level of alloying and fraction of precipitates provides only a moderate level of strengthening and enables planar slip to occur on multiple systems leading to a gradual change in crystallographic misorientations. When Mn and Mg are added, in the Al-Cu-Mn-Mg alloy, the density and equilibrium fraction of precipitates is increased thereby providing a higher degree of precipitate strengthening. This also appears to induce a more heterogeneous distribution of strain as the extent of slip becomes restricted and damage becomes more localized. The addition of Ag in 2139, catalyzes the formation of the Ω precipitate that serves to further increases the flow stress of the material. As these Ω precipitates appear to be finer and more resistant to dislocation shearing, planar slip distances during dynamic deformation are reduced even further. Compared to the two model alloys, the EBSD maps reveal the most localized damage and degree of intragranular misorientations are present in 2139. The magnitude of the misorientations changes as a function of the effective strain are also the largest in 2139. Interestingly, evidence of dynamic grain refinement occurring during deformation was also observed.

Appendix A: Modified Johnson-Cook Model

The widely used unmodified Johnson-Cook model gives the flow stress σ as:

$$\hat{\sigma}(\varepsilon_p, \dot{\varepsilon}, T) = [\sigma_0 + B(\varepsilon_p)^n] \left[1 + C \ln \left(\frac{\dot{\varepsilon}}{\dot{\varepsilon}_0} \right) \right] [1 - (T^*)^p] \quad (1a)$$

where normalized temperature is defined as:

$$T^* = \frac{T - T_0}{T_m - T_0} \quad (1b)$$

In this equation ε_p is the plastic strain, $\dot{\varepsilon}$ is the strain rate, $\dot{\varepsilon}_0$ is the reference strain rate, T_0 is a reference temperature and the T_m is the reference melting temperature. Other constants σ_0, B, n, C, p are Johnson-Cook model parameters defining yield stress, strain hardening terms, strain-rate dependency and thermal softening parameters, respectively.

This model, although widely available in commercial FE codes, is not refined enough to capture the experimental high strain rate and high temperature data for Al-Cu alloys in satisfactory manner. Therefore, we propose the following modifications to introduce temperature dependent strain hardening and strain-rate hardening coupled with seamless integration of dual strain rate regimes. The general form of the multiplicative decomposition of strain hardening, strain rate hardening and thermal softening terms is kept the same but the model parameters are modified as follows:

$$B = B_0 [1 - (T^*)^p] \quad (2a)$$

$$C = C_1 (T_r^*)^q + C_2 H(\varepsilon_p, \dot{\varepsilon}, k) \quad (2b)$$

$$T_r^* = \frac{T - T_0}{T_r - T_0} \quad (2c)$$

$$H(\varepsilon_p, \dot{\varepsilon}, k) = \frac{1}{2} + \frac{1}{2} \tanh \left(k \ln \left(\frac{\dot{\varepsilon}}{\dot{\varepsilon}_t} \right) \right) \quad (2d)$$

In the modified version of Johnson-Cook (MJC) model, the constant B accounts for temperature dependency of the strain hardening; this is typically observed in experiments. Model constant C introduces different slopes for the quasi-static and dynamic deformation regimes using a smoothed Heaviside step function. Due to the Heaviside step function only C_1 dominates the quasi-static regime, while C_2 dominates the high-strain-rate part. Again, this dual strain rate dependence is experimentally observed for the majority of engineering metals and alloys.

In the modified equations, term k represents the smoothness of the transition between quasi-static and dynamic regimes and is usually taken as 400. $\dot{\varepsilon}_t$ is the transition strain rate between the dynamic and the quasi static regimes. T_r is the room temperature.

The continuity of flow stress at the transition strain rate requires:

$$\hat{\sigma}_{qs}(\varepsilon_p, \dot{\varepsilon} = \dot{\varepsilon}_t, T) = \hat{\sigma}_{dyn}(\varepsilon_p, \dot{\varepsilon} = \dot{\varepsilon}_t, T) \quad (3a)$$

which leads to:

$$\dot{\varepsilon}_0 = \dot{\varepsilon}_{01} \left\{ 1 + \left[\left(\frac{\dot{\varepsilon}_t}{\dot{\varepsilon}_{01}} \right)^{\frac{c_2}{c_1(T_r^*)^p + c_2}} - 1 \right] H(\varepsilon_p, \dot{\varepsilon}, k) \right\} \quad (2b)$$

where $\dot{\varepsilon}_{01}$ is the reference strain rate that is typically taken as 10^{-4} s^{-1} .

Table A.1. Modified Johnson-Cook Model parameters for different materials

Material	q	σ_0	B_0	T_0	T_m	p	n	C_1	C_2	ε_{01}	ε_t	k
Poly. Al	2.9	14.5	140	175	780	1	0.45	0.0052	0.1565	0.001	20	400
Al-0.1Cu	3.9	5.5	112	41	670	3	0.36	0.0068	0.2065	0.001	150	400
Al-4.5Cu- 0.5Mg- 0.3Mn- 0.3Ag	4.5	426	234	0	640	3.9	0.2	0.0027	0.07	0.001	200	400

Table A.2. Zerilli-Armstrong Model parameters for different materials

Material	σ_a	A	C_0	α_1	α_2
Poly. Al	15	424	0.00000158489	0.0044	0.000225
Al-0.1Cu	17	390	0.00000501187	0.0039	0.000175

Table A.3. Turkkan-Vural Modified Zerilli-Armstrong Model parameters for different materials

Material	σ_a	p	T_0	T_m	ω	A	C_0	α_1	α_2
Al-4.5Cu- 0.5Mg-0.3Mn- 0.3Ag	0	4.5	160	625	14	460	0.00001	0.000175	0.0000275